POLITECNICO DI TORINO
Repository ISTITUZIONALE

Influence of base flow modelling and viscous effects on impedance eduction of acoustic liners

Original
Influence of base flow modelling and viscous effects on impedance eduction of acoustic liners / Paduano, A., Scarano, F., Bonomo, L.A., Casalino, D., Cordioli, J.A., Avallone, F.. - In: JOURNAL OF SOUND AND VIBRATION. - ISSN 0022-460X. - 649:(2027). [10.1016/j.jsv.2026.120228]

Availability:
This version is available at: 11583/3017868 since: 2026-11-13T07:48:16Z

Publisher:
Elsevier Science Limited

Published
DOI:10.1016/j.jsv.2026.120228

Terms of use:

This article is made available under terms and conditions as specified in the corresponding bibliographic description in the repository

Publisher copyright

(Article begins on next page)

21 November 2026

Journal of Sound and Vibration 649 (2027) 120228

Contents lists available at ScienceDirect

Journal of Sound and Vibration

journal homepage: www.elsevier.com/locate/jsvi

Influence of base flow modelling and viscous effects on impedance eduction of acoustic liners

Angelo Paduano [a,*], Francesco Scarano [a], Lucas A. Bonomo [b], Damiano Casalino [c], Julio A. Cordioli [b], Francesco Avallone [a]

[a] Department of Mechanical and Aerospace Engineering, Polytechnic of Turin, Corso Duca degli Abruzzi 24, Torino, 10129, TO, Italy
[b] Department of Mechanical Engineering, Federal University of Santa Catarina, R. Eng. Agronômico A. C. Ferreira s/n - Trindade, Florianópolis, 88040-900, SC, Brazil
[c] Flow Physics and Technology Department, Delft University of Technology, Mekelweg 5, Delft, 2628, CD, the Netherlands

ARTICLE INFO

Keywords:
Acoustic liner
Impedance
Eduction techniques

ABSTRACT

This work adopts a mid-fidelity numerical framework, coupling Reynolds-Averaged Navier-Stokes simulations with frequency-domain Linearised Navier-Stokes equations, to assess how conventional flow and acoustic propagation assumptions affect educed impedance. First, the approach is validated by simulating a three-dimensional acoustic liner geometry and comparing the results with experimental and high-fidelity scale-resolved simulation data. It is demonstrated that the framework reproduces the frequency-dependent acoustic impedance behaviour, capturing the impedance's directional dependence on acoustic wave propagation. However, differences in absolute values are present: there is a mean absolute error with respect to experiments of 0.09 on the normalised reactance and of 0.27 (upstream source) to 0.36 (downstream source) on the normalised resistance. Then, the liner geometry is substituted by an impedance wall boundary condition with a frequency-dependent impedance value equal to the one obtained from the explicit liner configuration. The impact on the acoustic field of assuming uniform flow with the Ingard-Myers boundary condition or a sheared flow with an impedance boundary condition without the thin boundary layer assumption is evaluated. It is found that, in both cases, the predicted transmitted and reflected fields remain direction-dependent, but the transmission–reflection partition depends on the selected combination of flow profile and acoustic formulation, with differences in the transmitted wave of up to 5 dB at fixed impedance. Based on this outcome, a FEM-based impedance-eduction method employing a dual-stage optimisation (global followed by local refinement) is introduced and applied with a shear-resolved, viscous forward model. Compared with a conventional uniform-flow eduction applied to the same acoustic field, this procedure reduces the propagation-direction difference in educed resistance from a maximum of $|\Delta\theta| \approx 0.40$ to $|\Delta\theta| \approx 0.18$.

1. Introduction

Acoustic liners are the most widely adopted technology for mitigating aircraft engine noise. From an engineering perspective, it is therefore essential to employ a parameter that depends solely on the liner geometry and the acoustic field conditions to characterise their performance. The parameter most commonly used for this purpose is the acoustic impedance, defined in the frequency domain as $Z(\omega) = \tilde{p}(\omega)/(\rho_0 c_0\, \tilde{\mathbf{u}}(\omega) \cdot \mathbf{n})$ where $\tilde{p}(\omega)$ denotes the complex acoustic pressure such that $p = \Re\left(\tilde{p}\, e^{i\omega t}\right)$. Similarly, $\tilde{\mathbf{u}}(\omega) \cdot \mathbf{n}$ is the complex

* Corresponding author.
E-mail address: angelo.paduano@polito.it (A. Paduano).

https://doi.org/10.1016/j.jsv.2026.120228
Received 23 March 2026; Received in revised form 14 October 2026; Accepted 24 October 2026
Available online 6 November 2026
0022-460X/© 2026 The Author(s). Published by Elsevier Ltd. This is an open access article under the CC BY-NC-ND license (http://creativecommons.org/licenses/by-nc-nd/4.0/).

wall-normal acoustic velocity, and ω is the frequency of the acoustic source. For locally reacting liners, impedance is defined as an intrinsic property of the surface, independent of the incident wave direction [1].

In realistic aeroengine environments, however, liners are subjected to high sound pressure levels (SPLs) and high-Mach-number grazing flows, conditions under which the determination of acoustic impedance becomes particularly challenging. Experimental investigations are typically restricted to relatively small test sections, and direct measurements of the near-wall acoustic velocity are extremely difficult. High SPLs and the presence of grazing flow lead to large velocity gradients near the liner surface, which severely complicates the velocity-based impedance calculation technique [2]. To date, direct impedance measurements are only possible using intrusive in-situ techniques [3,4], which are experimentally demanding, sensitive to the sampling location [5], and require microphones at the wall, which might perturb the local flow–acoustic interaction if not properly installed.

As a result, most studies rely on indirect approaches, commonly referred to as impedance-eduction methods. In these methods, the acoustic pressure is measured at several locations in the duct and a numerical propagation model is then used. In this case, the liner geometry is replaced by a spatially uniform impedance boundary condition. The acoustic field is reconstructed by solving a duct-acoustics model, most often the convected Helmholtz equation, supplemented with a wall boundary condition intended to account for the presence of a grazing mean flow. The liner impedance is obtained by minimising the mismatch between the measured and computed acoustic pressure fields.

Within this framework, the Ingard–Myers (IM) boundary condition [6,7] is by far the most widely adopted formulation. The IM model represents the boundary layer as an infinitesimally thin vortex sheet and enforces continuity of acoustic pressure and particle displacement across this sheet, while assuming zero mean flow on the wall side and a uniform mean flow in the outer region [8]. When employed in impedance eduction, the IM collapses the velocity variations near the wall into a single effective flow convective Mach number, typically defined using the bulk Mach number. Consequently, the detailed velocity gradients within the boundary layer, which are known to influence acoustic phase speeds, mode shapes, and evanescent behaviour, are not explicitly resolved. Instead, their effects are implicitly absorbed into the educed impedance $Z(\omega) = \theta + \mathrm{i}\chi$, where θ is the resistance and χ the reactance, which is obtained as the best match between computed and measured acoustic pressures. The resulting impedance, therefore, does not represent a purely intrinsic property of the liner's surface, but rather a compound quantity that depends on the liner's effective response, the specific shear-flow configuration under which it was measured, and the specific boundary condition to model an impedance in the presence of flow.

This blending fundamentally undermines one of the key assumptions underlying impedance-based liner characterisation: transferability. An impedance value educed under a given flow condition cannot, in general, be expected to remain valid when the shear profile, Mach number, or acoustic incidence changes [9]. From a modelling perspective, this raises a critical question: to what extent do the assumptions commonly used in impedance eduction techniques describe well liner physics?

A growing body of literature has demonstrated that explicitly accounting for the thickness and shape of the boundary layer is essential for accurate prediction of liner absorption [10,11]. Gabard [12], for example, compared the classical IM boundary condition with Brambley's formulation [13], which incorporates finite boundary-layer thickness, and reported substantial differences in predicted attenuation. Experimental studies have further shown that the acoustic impedance of liners subjected to grazing flow depends on the direction of acoustic wave propagation relative to the mean flow [14,15]. This directional dependence contradicts the locally reacting assumption and provides strong evidence that liner behaviour cannot be fully captured using a single, flow-independent impedance parameter.

These discrepancies point to a deeper issue: the extreme sensitivity of liner acoustic response to near-wall velocity gradients. They also cast serious doubt on the validity of the IM boundary condition for impedance eduction under realistic flow conditions, particularly when the boundary layer is neither thin nor weakly sheared. In such cases, the vortex-sheet approximation inherent to IM fails to represent the actual flow–acoustic coupling mechanisms near the liner surface [16].

The situation is further complicated by the fact that the IM condition is most often coupled with the inviscid convected Helmholtz equation, therefore omitting viscous effects in the acoustic field. Yet viscosity can play a non-negligible role in flow–acoustic interaction. In the presence of an oscillatory pressure field, an acoustically-induced boundary layer develops adjacent to the wall, consisting of fluid layers oscillating parallel to the surface. When viscous terms are neglected in the acoustic governing equations, the formation and influence of this layer are not represented. Aurégan et al. [16] showed that when the acoustic boundary layer is thin relative to the hydrodynamic shear layer, typically at high frequencies, the displacement continuity assumption underlying the IM condition provides an adequate approximation. As frequency decreases, the acoustic boundary layer thickens, and the displacement continuity assumption no longer holds [16]. Over porous surfaces such as acoustic liners [17], displacement continuity has been shown to fail across the entire frequency range [16]. Comparative studies based on the Linearised Navier–Stokes Equations (LNSE) and the Pridmore–Brown equation have further demonstrated that neglecting viscous effects can produce errors comparable in magnitude to those arising from neglecting the shear velocity profile itself [18,19].

Despite these insights, most existing investigations remain confined to canonical geometries such as cylindrical ducts or flat plates, and do not address the small ducts, strongly sheared, and geometrically complex flow environments characteristic of liner test rigs. As a result, the combined influence of strong shear-layer and viscous effects on impedance eduction remains poorly quantified.

Recent advances in high-fidelity numerical simulations have enabled more detailed investigations of near-wall flow–acoustic interactions. Zhang et al. [20] performed direct numerical simulations of laminar and turbulent boundary layers grazing a single-cavity liner under acoustic excitation, providing detailed insight into the fluid dynamics within and around the cavity. More recently, Paduano et al. [5] conducted lattice Boltzmann very-large-eddy simulations of turbulent flow over a multi-cavity liner subjected to varying acoustic forcing. They showed that abrupt surface modifications (such as the transition from a smooth wall to a lined surface) induce secondary motions that enhance wall-normal velocity fluctuations and increase the boundary layer displacement thickness.

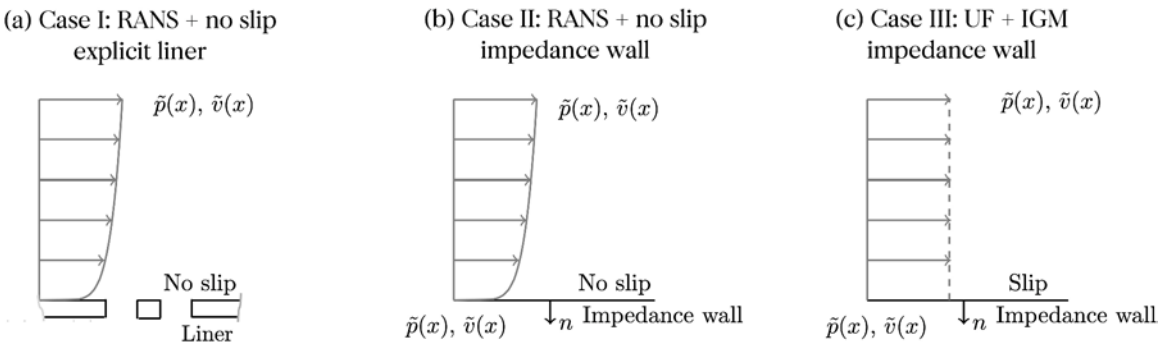


Fig. 1. Schematic illustration of acoustic wave propagation over an impedance boundary under three modelling approaches: (a) RANS mean flow coupled with LNSF solver using the explicitly resolved liner geometry; (b) RANS mean flow coupled with LNSF solver using a no-slip wall condition, $\tilde{u} = 0$; (c) uniform base flow profile combined with a slip boundary condition applied to the acoustic field, $U(y) = U_b$ and $\tilde{u} \neq 0$. In (c) the IM boundary condition is used, while in (b) an impedance wall boundary condition is adopted.

In the presence of acoustic excitation, the intensity of these motions depends on the relative orientation between the acoustic wave and the mean flow, resulting in pronounced spatial asymmetry of the flow field.

Complementary experimental evidence was provided by Roncen et al. [21], who employed laser Doppler velocimetry to measure acoustic-induced velocities above a liner subjected to high SPLs. They demonstrated that local impedance variations lead to strong amplifications of wall-normal acoustic velocity, giving rise to a spatially varying effective impedance along the liner surface. These observations directly challenge the common practice of representing a liner using a single, spatially uniform impedance and highlight the need to account for spatially evolving acoustic and hydrodynamic fields. Moreover, Paduano et al. [5] showed that when impedance is educed using the in-situ technique [3], the dependence of the educed impedance on the acoustic wave propagation direction is substantially reduced. Despite these advances, there remains a notable lack of impedance eduction techniques that do not rely on simplified boundary conditions to model near-wall flow–acoustic interactions. Weng et al. [22] developed an eduction framework based on the full LNSE, incorporating viscothermal effects and applied it to duct experiments with grazing flow. Although their approach accounts for viscous acoustics, the educed impedance was still found to depend on the direction of acoustic wave propagation relative to the mean flow. This suggests that even LNSE-based equivalent-boundary formulations cannot fully disentangle intrinsic liner properties from flow-induced effects. However, their study does not include a systematic comparison between educed impedances and reference acoustic fields obtained from explicitly resolved liner geometries, which is essential to isolate the respective contributions of shear-flow profiles and viscous effects.

This reveals a critical gap between the flow–acoustic physics resolved in high-fidelity simulations or local measurements and the simplified equivalent-impedance descriptions commonly adopted for design and analysis. In particular, the separate contributions of the mean shear profile and of the acoustically induced viscous boundary layer to the educed impedance remain insufficiently quantified, especially as a function of acoustic wave propagation direction.

The objective of this work is to assess how much of the high-fidelity impedance-eduction response can be recovered with reduced-complexity models, and to determine the minimum modelling fidelity required to achieve comparable results. To this end, we adopt a mid-fidelity computational framework that combines Reynolds-averaged Navier–Stokes (RANS) simulations for the mean flow with frequency-domain linearised Navier–Stokes equations (LNSF) [23] for the acoustic perturbations. This coupled approach provides a detailed yet computationally tractable description of the interaction between the acoustic field and the near-wall flow.

A systematic comparison is then performed across two duct-acoustics propagation models: (i) a fully resolved sheared mean-flow profile, obtained from RANS simulations, coupled with LNSF with an impedance boundary condition; (ii) a uniform-flow coupled with a potential-flow formulation, where the IM condition is used. By comparing the acoustic field over the impedance wall from these configurations, the present study isolates and quantifies the impact of shear, boundary-layer modelling, and viscous effects on impedance eduction, and identifies when and why widely used simplifications break down. Finally, a dedicated Finite Element Model (FEM) based impedance-eduction technique is developed and validated against the LNSF reference solutions. Fig. 1 presents a schematic representation of the different boundary conditions employed for the three cases.

The remainder of the paper is structured as follows. Section 2 details the methodology; Section 3 shows the different acoustic models tested using an impedance boundary condition. Sections 4 and 5 present and discuss the results, while Section 6 presents the FEM-based eduction technique. The main conclusions are summarised in Section 7.

2. Methodology

2.1. Solver

The calculation employs a FEM framework and consists of two main steps: a RANS simulation of the mean flow, followed by a frequency-domain aeroacoustic analysis that solves the acoustic field in the presence of grazing flow. All simulations were performed

in COMSOL Multiphysics 6.3, driven through a Python interface code. The computational process begins with computing the RANS solution, where the turbulent (eddy) viscosity (ν_T) is computed using Menter's Shear Stress Transport (SST) turbulence model [24].

Once the mean flow is established, the acoustic analysis is conducted using the LNSF solver. Here, acoustic perturbation superimposed on the mean flow is expressed in harmonic form:

$$\tilde{p} = A\mathrm{e}^{-\mathrm{i}k^{\pm}x}, \tag{1}$$

where A is the amplitude of the acoustic wave, and the wavenumber is defined as $k^{\pm} = \frac{\pm\omega}{c_0(1\pm M_b)}$, where c_0 is the speed of sound. The $\pm$ sign accounts for the propagation direction relative to the mean flow: the plus sign corresponds to downstream propagation (in the same direction as the flow), whereas the minus sign corresponds to upstream propagation (in the direction opposite to the flow).

The governing equations for the LNSF solver are linearised around the steady mean flow $\mathbf{U}$, pressure p_0, density ρ_0 and temperature T_0, and expressed in the frequency domain by substituting time derivatives with multiplication by $\mathrm{i}\omega$. Introducing the linearised material derivative

$$\mathrm{D}(\cdot) \;=\; \mathrm{i}\omega\,(\cdot) \;+\; (\mathbf{U}\cdot\nabla)(\cdot), \tag{2}$$

the governing equations include conservation of mass, momentum, and energy with viscous, thermal, and convective effects, read:

$$\mathrm{i}\omega\,\tilde{\rho} + \nabla\cdot\left(\tilde{\rho}\,\mathbf{U} + \rho_0\,\tilde{\mathbf{u}}\right) = 0, \tag{3}$$

$$\rho_0[\mathrm{D}\tilde{\mathbf{u}} + (\tilde{\mathbf{u}}\cdot\nabla)\mathbf{U}] + \tilde{\rho}\,(\mathbf{U}\cdot\nabla)\mathbf{U} = \nabla\cdot\tilde{\boldsymbol{\sigma}}, \tag{4}$$

$$\rho_0 c_p\,\mathrm{D}\tilde{T} - \alpha_T T_0\,\mathrm{D}\tilde{p} = \nabla\cdot(k_{\mathrm{th}}\nabla\tilde{T}) + \tilde{\Phi}, \tag{5}$$

$$\tilde{\rho} = \rho_0\left(\beta_T\,\tilde{p} - \alpha_T\,\tilde{T}\right), \tag{6}$$

where the superscript $\tilde{(\cdot)}$ denotes the complex amplitude of the acoustic perturbation, α_T, β_T and k_{th} are the thermal expansion coefficient, isothermal compressibility and thermal conductivity, respectively. $\tilde{\boldsymbol{\sigma}}$ and $\tilde{\Phi}$ are the perturbation stress tensor and the linearized viscous dissipation function, respectively. The perturbation stress tensor is:

$$\tilde{\boldsymbol{\sigma}} \;=\; -\tilde{p}\,\mathbf{I} + \mu(\nabla\tilde{\mathbf{u}} + (\nabla\tilde{\mathbf{u}})^{\mathrm{T}}) + (\mu_B - \tfrac{2}{3}\mu)(\nabla\cdot\tilde{\mathbf{u}})\mathbf{I}, \tag{7}$$

where μ and μ_B are the molecular and the bulk viscosities, respectively. The linearised viscous dissipation term is defined as:

$$\tilde{\Phi} = \nabla\tilde{\mathbf{u}} : \boldsymbol{\tau}(\mathbf{U}) + \nabla\mathbf{U} : \boldsymbol{\tau}(\tilde{\mathbf{u}}), \tag{8}$$

$$\boldsymbol{\tau}(\tilde{\mathbf{u}}) = \mu\left(\nabla\tilde{\mathbf{u}} + (\nabla\tilde{\mathbf{u}})^{\mathrm{T}}\right) + \left(\mu_B - \tfrac{2}{3}\mu\right)(\nabla\cdot\tilde{\mathbf{u}})\mathbf{I}, \tag{9}$$

$$\boldsymbol{\tau}(\mathbf{U}) = \mu\left(\nabla\mathbf{U} + (\nabla\mathbf{U})^{\mathrm{T}}\right) + \left(\mu_B - \tfrac{2}{3}\mu\right)(\nabla\cdot\mathbf{U})\mathbf{I}. \tag{10}$$

In regions of strong shear, coherent acoustic perturbations are additionally damped by the background turbulence, an effect that must be represented in the viscous terms of Eqs. (4) and (5). The rationale follows the triple decomposition of Reynolds and Hussain [25], in which the instantaneous flow field is split into a time-averaged, a coherent and a random turbulent part:

$$u_i(\mathbf{x},t) \;=\; U_i(\mathbf{x}) \;+\; u_i^c(\mathbf{x},t) \;+\; u_i'(\mathbf{x},t), \tag{11}$$

where $(\cdot)^c = \langle\cdot\rangle - \overline{(\cdot)}$ represents the coherent component in the time domain, with $\langle\cdot\rangle$ and $\overline{(\cdot)}$ denoting the phase- and time-averaging operators, respectively, and $(\cdot)'$ denotes the random turbulent fluctuation, which vanishes under phase averaging. Applying this decomposition to the Navier-Stokes equations, phase-averaging and subtracting the time-averaged equations yields an additional unclosed term in the coherent momentum equation,

$$r_{ij}^c \;=\; \langle u_i' u_j'\rangle \;-\; \overline{u_i' u_j'}. \tag{12}$$

This term represents the oscillation of the turbulent Reynolds stresses induced by the coherent acoustic field. Retaining only the component at the forcing frequency, the coherent quantities are expressed through their complex amplitudes as $u_i^c = \Re\{\tilde{u}_i\,\mathrm{e}^{\mathrm{i}\omega t}\}$ and $r_{ij}^c = \Re\{\tilde{r}_{ij}\,\mathrm{e}^{\mathrm{i}\omega t}\}$. Following [25], it is modelled through a Newtonian eddy closure:

$$\tilde{r}_{ij} \;=\; -\nu_T\left(\frac{\partial\tilde{u}_i}{\partial x_j} + \frac{\partial\tilde{u}_j}{\partial x_i} - \frac{2}{3}\,\frac{\partial\tilde{u}_k}{\partial x_k}\,\delta_{ij}\right), \tag{13}$$

which assumes an instantaneous, in-phase response of the turbulent stresses to the coherent strain rate, thereby neglecting any relaxation time or phase lag of the background turbulence, and adopts the same eddy viscosity as the mean flow. Under this closure, Eq. (13) is formally equivalent to an additional viscous stress, so that the molecular dynamic viscosity in the LNSF equations is simply augmented as $\mu + \rho_0\nu_T$. The resulting contribution is dissipative and accounts for the damping of coherent perturbations by the background turbulence, which cannot in general be neglected in regions of strong shear [25]. In the present implementation, ν_T is frozen from the steady RANS solution: the acoustic field does not modify the background turbulence intensity, consistently with the one-way coupling adopted in this work. The effectiveness of this approach in frequency-domain LNSF computations was demonstrated by Holmberg et al. [26], who reported improved agreement with experimental scattering data when eddy-viscosity damping is included; note that the closure is agnostic with respect to the turbulence model employed to obtain ν_T.

Table 1
Summary of mesh parameters for the fluid dynamic and acoustic simulations. $\Delta y^+_{\min} = \Delta y_{\min} u_\tau/\nu$ is the height of the first wall cell in wall units, with u_τ the friction velocity. The number of elements across the acoustic viscous sublayer thickness δ_v is evaluated at the highest frequency tested ($f = 2500$ Hz).

Mesh type	Number of elements	Re_b	$\Delta y^+_{\min}$	Elements across δ_v
Tetrahedral	1.2×10^6	2.7×10^5	1.10	10

Moreover, the weakly-coupling assumption is supported by the high-fidelity simulations of Paduano et al. [5], performed on the same liner geometry and flow conditions, which show that the modification of the time-averaged velocity profile induced by the acoustic excitation remains below 4% at the trailing edge of the liner, even at the highest SPL considered here (145 dB); the near-wall mean-flow modification is instead dominated by the presence of the lined surface itself. However, in terms of time-dependent quantities, the SPL modify the unsteady near-wall flow behaviour [5,27]; in this sense, the present framework is not intended as a substitute for fully coupled, time-resolved simulations; it is a mid-fidelity tool to educe the impedance and to obtain a low-cost approximation of the frequency-dependent behaviour of the liner.

Spatial discretisation is performed using FEM, with pressure discretised linearly and velocity and temperature discretised with quadratic Lagrange elements for improved accuracy. The solution of the LNSF produces the complex acoustic field describing steady-state acoustic wave propagation, including viscous, thermal, and convective effects around the liner geometry.

The resulting efficiency allows an extended frequency range to be investigated, from 700 Hz to 2500 Hz. This range was selected to capture the liner behaviour before, near, and slightly beyond the resonance frequency. All cases share the amplitude of the incident acoustic wave corresponding to an SPL of 145 dB.

2.2. Mesh design

The computational mesh was designed to accurately resolve the near-wall flow region, which plays a key role in the mechanisms of acoustic energy absorption. An unstructured mesh consisting of tetrahedral elements has been employed, with local refinement near the wall and progressive coarsening toward the channel centre, as depicted in Fig. 2(b).

For instance, the configuration considered—an impedance wall (either an explicit liner or a uniform impedance boundary condition) exposed to a grazing flow with centreline Mach number $M_{\text{cl}} = U_\infty/c_0 = 0.32$, where U_∞ is the centreline velocity, and bulk Reynolds number $Re_b = 2.7 \times 10^5$, together with acoustic excitation—constitutes a multiscale problem. In the channel core, a relatively coarse spatial resolution is sufficient to capture acoustic-wave propagation. By contrast, the near-wall region requires a much finer mesh to resolve the strong velocity gradients associated with the hydrodynamic boundary layer, which are known to influence flow–acoustic interactions [5,28].

Moreover, in the presence of an oscillatory pressure field, the acoustic-induced boundary layer forms adjacent to the wall. Its physical origin is analogous to the classical Stokes oscillatory layer: when the outer flow oscillates harmonically, viscous diffusion prevents the no-slip condition from being satisfied instantaneously at the wall, leading to the formation of a thin region in which velocity gradients are confined. This layer has a characteristic thickness δ_v given by Berggren et al. [29]:

$$\delta_v = \sqrt{\frac{2\nu}{\omega}}, \tag{14}$$

where ν is the kinematic viscosity.

To adequately resolve this layer, prism-layer elements were employed in the near-wall region, with grid spacing increasing in the wall-normal direction. For the highest frequency tested ($f = 2500$ Hz), the mesh provides at least 10 grid points across δ_v.

The mesh topology guarantees a smooth transition between adjacent regions, particularly in zones of flow acceleration and near the orifices, to prevent excessive skewness that could compromise solution accuracy.

A summary of the principal mesh parameters is reported in Table 1. A dedicated mesh convergence analysis, detailed in Appendix A, confirmed that further refinement did not lead to appreciable variations in the flow field nor in the impedance eduction results.

3. Test cases

To systematically isolate the influence of the sheared mean-flow profile and viscous effects on the acoustic field, three configurations are investigated. As discussed in the Introduction and illustrated in Fig. 1, the first configuration consists of a fully resolved simulation of the flow over an explicit liner, where the mean flow is obtained from RANS and the acoustic field is solved using the LNSF formulation. This case serves as the reference solution.

In the second configuration, the same sheared mean-flow profile obtained from the RANS simulations is retained, but the liner geometry is replaced by an impedance boundary condition while the acoustic field is still solved with the LNSF equations. The third configuration represents a simplified model in which the mean flow is assumed uniform and the acoustic propagation is described by a potential-flow formulation, with the IM boundary condition used to represent the flow–acoustic interaction at the wall. These

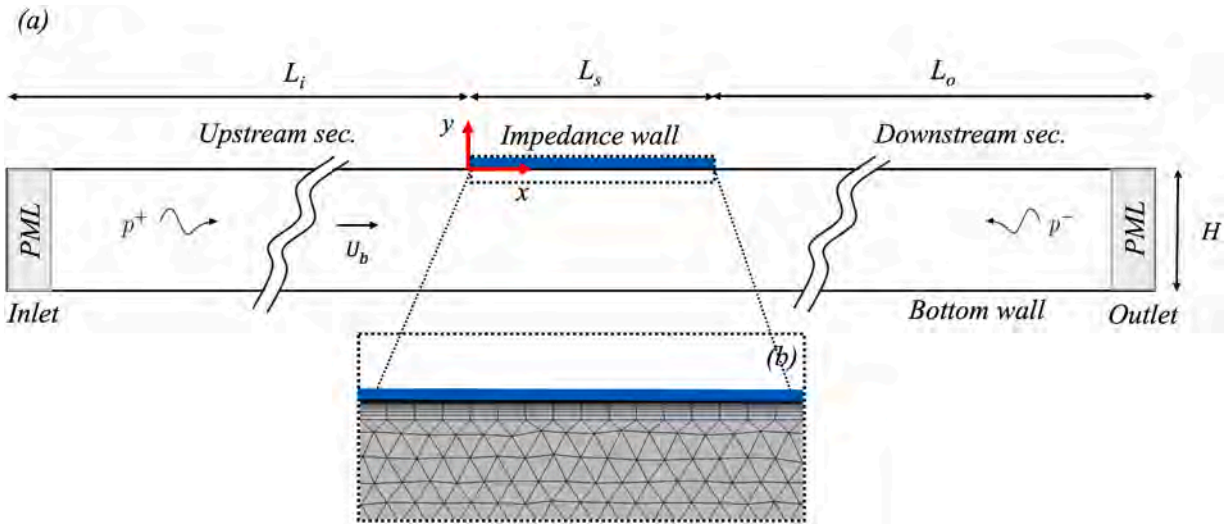


Fig. 2. (a) Schematic of the computational domain, (b) detail of the near-wall mesh.

configurations, therefore, span a range of modelling fidelities, from an explicitly resolved liner to simplified impedance-based descriptions. This comparative approach allows the validity range of simplified flow–acoustic models—such as the uniform-flow slip condition—to be assessed for predicting near-wall flow–acoustic coupling.

It is important to emphasise that the simplified models employed here are not intended to predict changes in liner impedance induced by the mean flow. Instead, they are used to quantify how the presence of a sheared mean flow and viscous effects modifies the acoustic field in the vicinity of a treated surface when a prescribed wall impedance is imposed.

3.1. Computational domain

The computational domain, depicted in Fig. 2, consists of a grazing flow impedance tube bounded at both ends by Perfectly Matched Layers (PMLs) [30] to ensure fully absorptive boundary conditions and reduce acoustic reflections. The channel has a height $H = 2h = 40\,\text{mm}$, with upstream and downstream lengths $L_i = L_o = 350\,\text{mm}$ chosen to allow at least one acoustic wavelength before the liner for the lowest frequency of interest. The spanwise width of the domain is $L_z = 12.44\,\text{mm}$, and periodic boundary conditions are applied in this direction. At the inlet, a fully developed flow boundary condition is imposed, corresponding to a bulk Mach number of $M_b = U_b/c_0 = \frac{1}{2hc_0}\int_0^{2h} U(y)dy = 0.296$, where $U(y)$ is the fully developed flow profile. $L_s = 136\,\text{mm}$ is the length of the impedance wall. At the outlet, a pressure gauge boundary condition and PML are applied. The reflections from the non-reflecting boundary conditions have been computed by dividing the magnitude of the waves incident on the inflow or outflow boundaries by those propagating from the corresponding boundary. It has been observed that the PMLs reflect less than 0.3% of the incident energy for the frequencies tested, in agreement with previous studies [31].

3.2. Explicit liner

The first configuration under investigation features an explicitly resolved liner reported in Fig. 3. In this case, the mean flow is solved using RANS, while the acoustic field is solved using the LNSF approach. The liner geometry tested is the one characterised experimentally by Quintino et al. [9] and numerically by Paduano et al. [5]. The liner is installed along the upper wall of a channel, as depicted in Fig. 2. It consists of eleven cavities arranged in series, extending over a total length of $L_s = 136\,\text{mm}$. This length is shorter than that used in the experimental campaign of Quintino et al. [9]. The reduction is motivated by computational cost considerations, following the approach adopted in previous numerical studies [5]. Each cavity features a square cross-section with a width of $l = 9.90\,\text{mm}$ and a depth of $H_c = 38.10\,\text{mm}$. Within each cavity, eight orifices with a diameter $d = 1.17\,\text{mm}$ are separated by partition walls of thickness $w_p = 1.27\,\text{mm}$; the facesheet enclosing the cavities has a thickness of $\tau = 0.54\,\text{mm}$. To more accurately replicate the physical liner sample, the simulated geometry includes a slight rounding of the edges, as in the manufactured sample. This geometry was reconstructed using a high-resolution 3D scanning technique.

3.3. Fully resolved boundary layer with no-slip acoustic condition

For test case II (Fig. 1b), the analysis begins with the computation of the mean flow field, obtained via a RANS simulation of the smooth channel. This setup allows the boundary layer to develop naturally, resulting in a canonical fully developed channel flow. The resulting base flow profile,

$$\mathbf{U}(y) = [U(y), 0, 0], \tag{15}$$

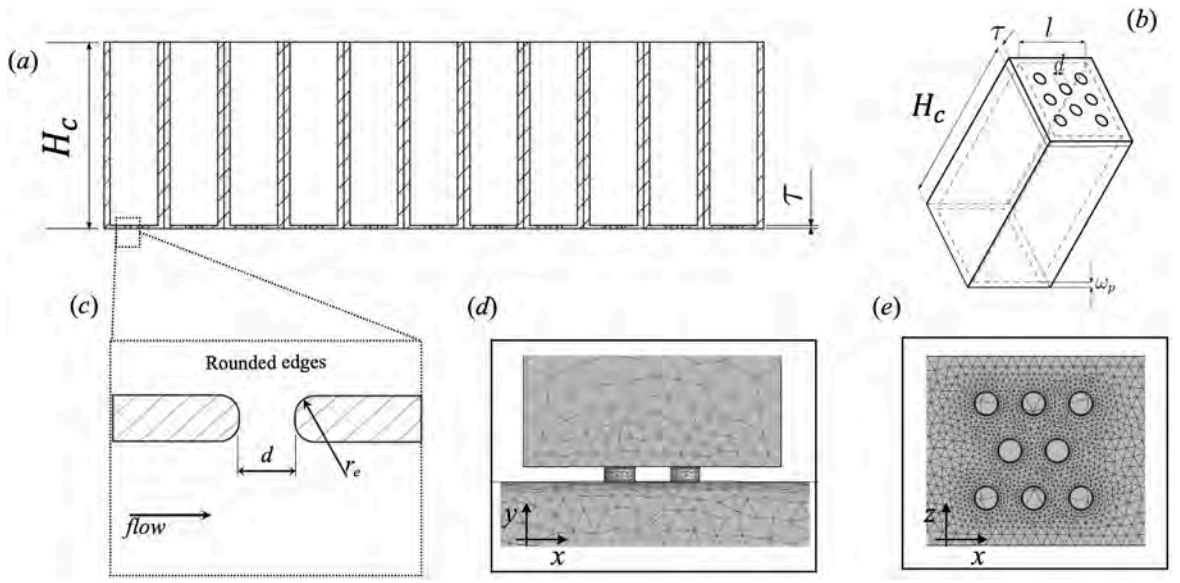


Fig. 3. Schematic representation of the liner sample: (a) full liner geometry; (b) detailed view of a cavity with dimensions; (c) detailed view of the orifice shape; near-orifice mesh views in a *x*-*y* plane (d) and *x*-*z* plane (e).

is subsequently coupled to the acoustic solver as a frozen background state.

For the acoustic field, the explicit liner geometry is replaced by a uniform impedance boundary condition with a prescribed uniform impedance:

$$Z_{\mathrm{eff}}(\omega) = \frac{\tilde{p}(\omega)}{\rho_0 c_0 \tilde{\mathbf{u}}(\omega) \cdot \mathbf{n}} \tag{16}$$

This impedance imposes a specific relationship between acoustic pressure and wall-normal particle velocity for a fixed SPL. The IM boundary condition is not employed in this setup. Instead, because the viscous boundary layer is resolved in the mean flow, the acoustic field is subject to a standard no-slip condition on the tangential velocity component:

$$\tilde{u} = 0 \quad \text{at the wall,} \tag{17}$$

while the non-zero wall-normal velocity is governed solely by the prescribed impedance.

3.4. Uniform mean flow with slip acoustic condition

In the third configuration (Fig. 1c), the sheared flow profile is replaced by a uniform velocity:

$$U(y) = U_b. \tag{18}$$

The same slip boundary condition is applied to the acoustic field. Since in this case the viscosity is neglected, the acoustic field is then governed by the convected Helmholtz equation:

$$\nabla^2 \tilde{p} + k_0^2 \left(1 - M_b^2 \cos^2 \Theta\right) \tilde{p} = 0, \tag{19}$$

where $k_0 = \omega / c_0$ is the free-field wavenumber and Θ is the incident wave angle. In the present work, only axial plane-wave propagation is considered, so that $\Theta = 0$ for upstream source location and $\Theta = \pi$ for downstream source location; no oblique or higher-order modal incidence is investigated. In this configuration, the IM condition [6,7] is implemented to model the acoustic flow interaction near the wall in the presence of a shear flow profile. The impedance boundary condition reads in this case:

$$Z_{\mathrm{eff}}(\omega) = \frac{Z(\omega)}{1 - M_b k_x / k_0}. \tag{20}$$

4. Validation of the flow field and educed impedance for the explicit liner

In the remainder of the paper, the three cases described in the previous section will be considered. However, since the explicit liner case is treated as the reference, first an extended validation of this case against both experimental and high-fidelity numerical results for the same liner geometry [5,9] is provided.

4.1. Mean flow

The computed mean flow field for the explicit liner is first assessed against the high-fidelity reference data of Paduano et al. [5]. Fig. 4 shows the mean streamwise velocity profiles at three streamwise positions along the liner: inlet ($x/L = 0$), mid-length ($x/L = 0.5$), and outlet ($x/L = 1$). The high-fidelity data were sampled at the same streamwise locations. Notably, the velocity profile at the liner entrance matches closely with the reference dataset, demonstrating that the employed methodology reproduces reference flow conditions within the test section.

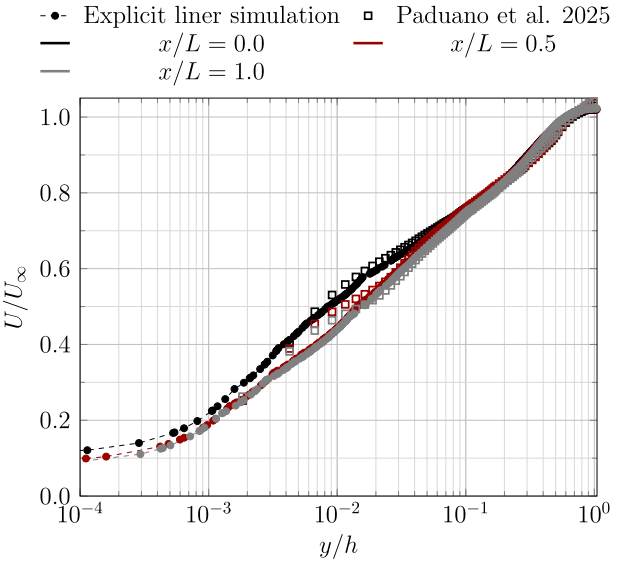


Fig. 4. Mean flow profile compared with high-fidelity simulation by Paduano et al. [5].

As the flow develops over the liner surface, a progressive near-wall velocity deficit, consistent with the reference data, is observed. This velocity deficit mainly develops within the first half of the liner, as evidenced by the minimal changes in velocity profiles between $x/L = 0.5$ and $x/L = 1$. This evolution aligns well with previous observations [5,32], confirming that the streamwise development of the shear velocity profile over the liner is properly captured. Minor discrepancies arise in the wall-normal region $3 \times 10^{-3} < y/h < 7 \times 10^{-3}$, where the RANS predictions slightly overestimate the velocity deficit.

4.2. Impedance

Fig. 5(a) and (b) present impedance values normalised with respect to air impedance ($\rho_0 c_0$) compared against experimental measurements and numerical results from the literature [5,9] for the explicit liner. Both source locations, i.e. upstream and downstream, are reported. To ensure robust validation, the same eduction technique employed in the literature is used here. For instance, the Mode Matching Method (MM) [14,33] is employed, and particular care is taken to match the same number of microphones and their locations.

In Fig. 5(a), the educed resistance decreases in magnitude with increasing frequency for all configurations, in agreement with the general trend observed in both experiments and high-fidelity simulations. However, the resistance is systematically underestimated over the entire frequency range. Quantitatively, for the upstream source case the mean absolute error of the resistance computed as $|(\theta_{experimental} - \theta_{simulations})|$ is 0.27, with a maximum deviation of 0.31 at $f = 1700$ Hz, close to the resonance frequency of the liner in the presence of flow; the reactance is captured within a mean absolute error of 0.09. The underestimation is systematic rather than random: it shifts the absolute resistance level while preserving its frequency dependence and the propagation-direction difference $|\Delta\theta|$ on which the present analysis relies. This discrepancy is likely related to limitations of the present modelling framework, in which the coupling between the acoustic field and the underlying flow dynamics remains weak and the acoustic field is resolved by means of linearised Navier- Stokes equations, as described in Section 2. In particular, additional dissipation mechanisms associated with flow unsteadiness, and local non-linear effects known to increase the effective resistance [34,35] are not explicitly represented. For the upstream-source case, the nonlinear resistance contribution estimated with the semi-empirical model of Yu et al. [34] matches the gap between experimental and computed resistance in both magnitude (mean ≈ 0.23) and frequency trend as described in B; for the downstream source no equivalent model is available, although the offset (≈ 0.36) retains the same nearly constant, frequency-preserving character, suggesting a common origin.

Fig. 5(b) shows that the frequency-dependent behaviour of the reactance is well reproduced when compared with experimental and high-fidelity data. The predicted trends closely follow the reference datasets across the investigated frequency range, indicating that the reactive component of the liner response is well captured.

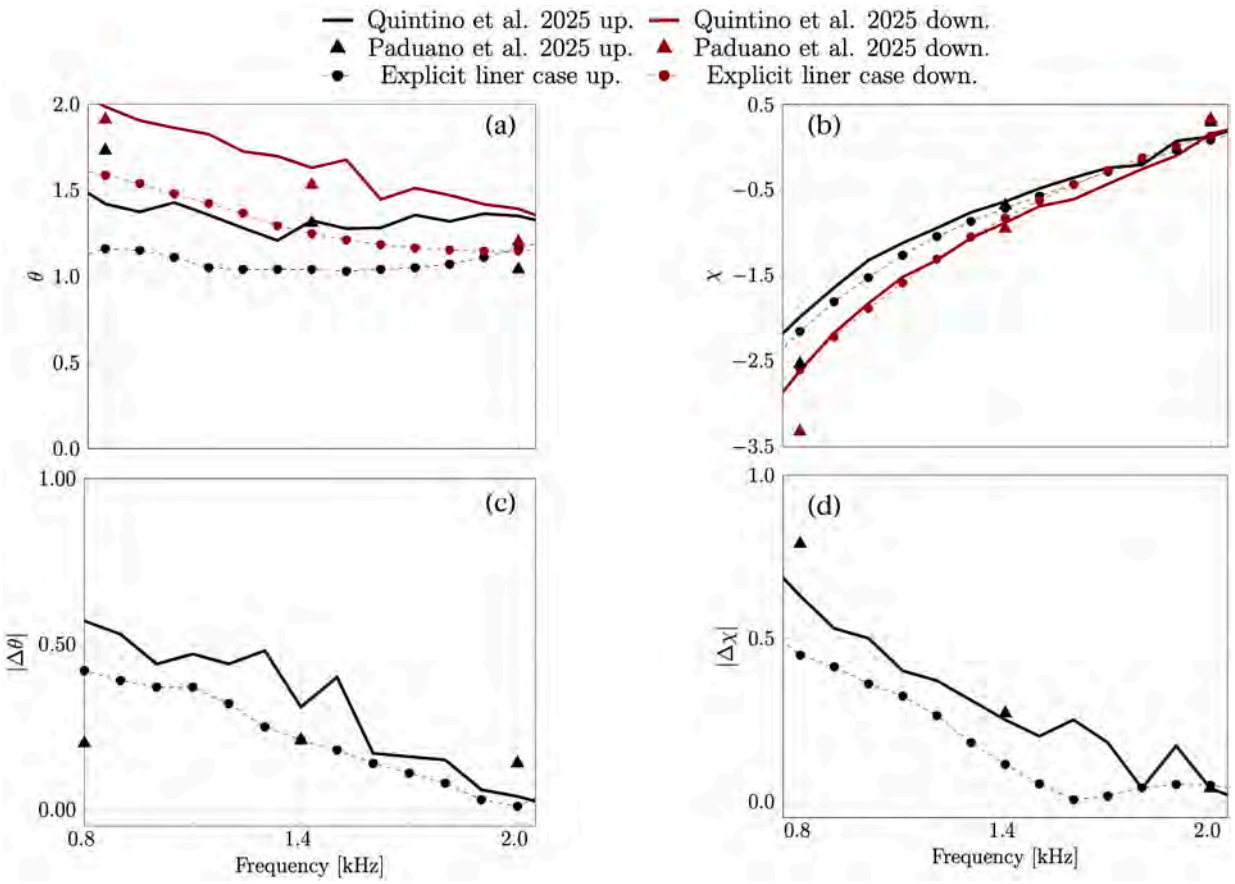


Fig. 5. Comparison of impedance results from the explicit liner simulation against the experimental results of Quintino et al. [9] and the numerical results of Paduano et al. [5]. (a) Resistance, (b) Reactance, (c) resistance difference as $|\Delta\theta| = |\theta_{\text{down}} - \theta_{\text{up}}|$, and (d) reactance difference as $|\Delta\chi| = \left||\chi_{\text{down}}| - |\chi_{\text{up}}|\right|$.

Both resistance and reactance exhibit a clear dependence on the acoustic-wave propagation direction. These behaviours are consistent with previously validated experimental and numerical results [4,5,36], confirming that the present methodology captures the combined influence of frequency and propagation direction on the liner impedance.

To further assess the capability of the framework to reproduce direction-dependent effects, Fig. 5(c) and (d) report $|\Delta\theta| = \left||\theta_{\text{down}}| - |\theta_{\text{up}}|\right|$ and $|\Delta\chi| = \left||\chi_{\text{down}}| - |\chi_{\text{up}}|\right|$, where "down" and "up" denote downstream and upstream source locations, respectively. Experimental data show a modest increase of $|\Delta\theta|$ at low frequencies, in agreement with simulations, indicating that the main mechanisms driving the resistance difference are captured. The remaining mismatch between numerical and experimental results at the lowest frequencies may be attributed to finite-duct effects and to the different ratio between liner length and acoustic wavelength in the experiments, which leads to a more pronounced SPL decay at low frequencies [9].

$|\Delta\chi|$ exhibits close agreement across datasets, with only minor frequency shifts observed in the present results. This behaviour can be interpreted through the mass–spring analogy of resonator liners, in which χ reflects the balance between inertial (mass) and stiffness contributions. The stiffness is primarily dictated by cavity depth, whereas the effective inertance depends on end-correction terms that are sensitive to grazing-flow conditions and propagation direction [37,38]. In the present framework, the acoustic field is treated as linear and weakly coupled to the mean flow, as detailed in Section 2. Consequently, two physical mechanisms that modulate the reactance are inherently neglected: (i) nonlinear acoustic–vortex interactions at the orifice, which would otherwise alter the effective mass of the oscillating fluid; and (ii) the modification of the streamwise velocity deficit by the acoustic wave propagation direction, as demonstrated by Paduano et al. [5]. Cumulatively, the exclusion of these effects modifies the effective oscillating fluid volume near the orifice. This modification might shift the frequency at which the reactance difference, $|\Delta\chi|$, crosses zero, leading to the slight offsets observed in the results.

As an additional validation, Fig. 6 compares the SPL decay along the lined section with high-fidelity results for three representative frequencies and both propagation directions. The SPL decay predicted by the present framework has been compared quantitatively with the high-fidelity data for all three frequencies and both propagation directions. The LNSF results were sampled at the same streamwise stations as the high-fidelity data, and the local error was defined as $e(x) = \text{SPL}_{\text{LNSF}}(x) - \text{SPL}_{\text{HF}}(x)$. From this, the mean

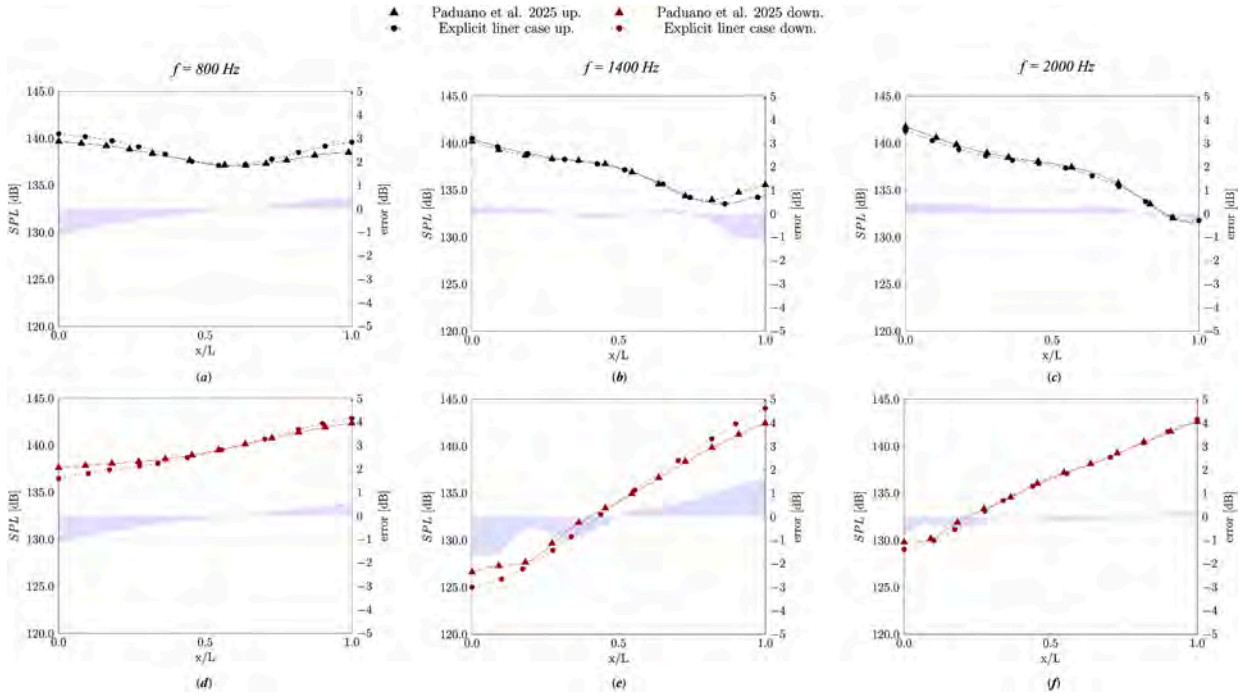


Fig. 6. SPL decay at three frequencies compared with high-fidelity data from Paduano et al. [5]. The shaded blue area (right axis) is the local error $e = \mathrm{SPL}_{\mathrm{LNSF}} - \mathrm{SPL}_{\mathrm{HF}}$. Top row, upstream source location; bottom row, downstream source location. (For interpretation of the references to colour in this figure legend, the reader is referred to the web version of this article.)

absolute error (MAE) and the maximum error over the whole liner and the MAE over the central region ($0.2 \leq x/L \leq 0.8$) were computed. The present simulations reproduce the overall decay rates and the directional trends with an MAE from 0.20 to 0.84 dB. Minor differences appear at the liner's beginning and end, which may correspond to the subtle variations in wall impedance observed in Fig. 5. The largest deviation of 1.72 dB occurs for the 1400 Hz case and downstream source at the beginning of the lined section. However, the decay slopes along the central region of the liner remain consistent with the reference data: in this region, the MAE drops to between 0.11 dB and 0.55 dB, obtained for the upstream and downstream source at 1400 Hz, respectively. At 2000 Hz, the SPL distributions closely align with reference data, consistent with the reduced impedance discrepancies observed in Fig. 5(a) and (b). At this frequency, the MAE in the central region is 0.25 and 0.13 dB for the upstream and downstream source locations, respectively. Collectively, these results provide an extensive validation of the numerical framework, demonstrating that the present approach captures the dependence on both frequency and acoustic-wave propagation direction, while highlighting the remaining limitations, which are primarily associated with the resistive component, despite the substantially reduced computational cost. Appendix F reports a detailed comparison of the computational cost with respect to high-fidelity simulations.

5. Uniform impedance: impact of flow profile and acoustic modelling

The investigation proceeds to assess the practical use of the educed impedance values as boundary conditions in simplified acoustic models. In this section, the liner is replaced by a smooth impedance wall whose area matches the liner surface. Fig. 7 compares the mean-flow profiles used in the impedance-boundary simulations with the profile extracted at the downstream end of the fully resolved liner simulation; all share the same bulk Mach number of 0.296. However, the impedance-boundary simulations are hydrodynamically smooth, leading to a different flow profile. For instance, the fully resolved liner case exhibits a clear near-wall velocity deficit that is not present when the liner is replaced by a smooth impedance boundary. This difference is consistent with the physical development of the mean flow over a perforated liner: interaction with the orifices and the associated momentum exchange alter the near-wall region and can locally reduce the mean velocity [5,17,32,39]. Such effects are absent in the impedance-boundary configuration, where the surface is assumed smooth, and the mean-flow development is therefore not influenced by the liner geometry. The implications of neglecting this modification of the mean velocity profile are discussed in the remainder of the paper.

The impedance imposed on this wall is taken from the MM eduction [14,33] performed for the upstream-source configuration (black markers in Fig. 5(a,b)). The selection of the upstream-source impedance is not intended to be unique; instead, it provides a fixed and consistent reference impedance used in the remainder of the paper. This controlled setup ensures that differences in the predicted acoustic field can be attributed to the modelling assumptions (base-flow representation and propagation model), rather than to variations in the imposed wall impedance.

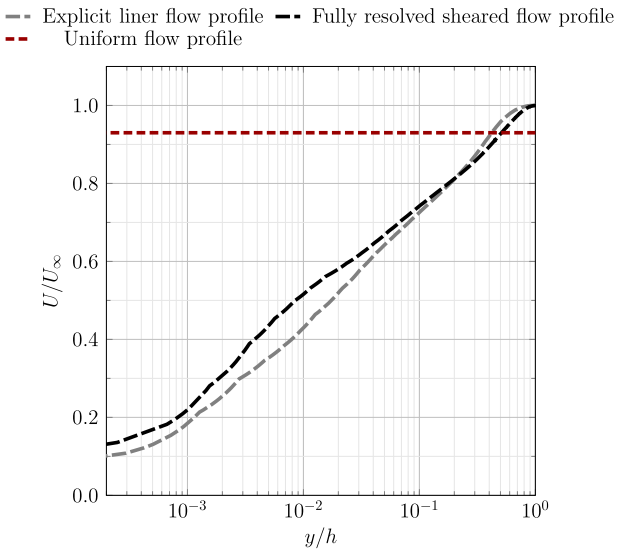


Fig. 7. Mean-flow profiles used in the impedance-boundary simulations, compared with the mean-flow profile extracted at the downstream end of the fully resolved liner simulation.

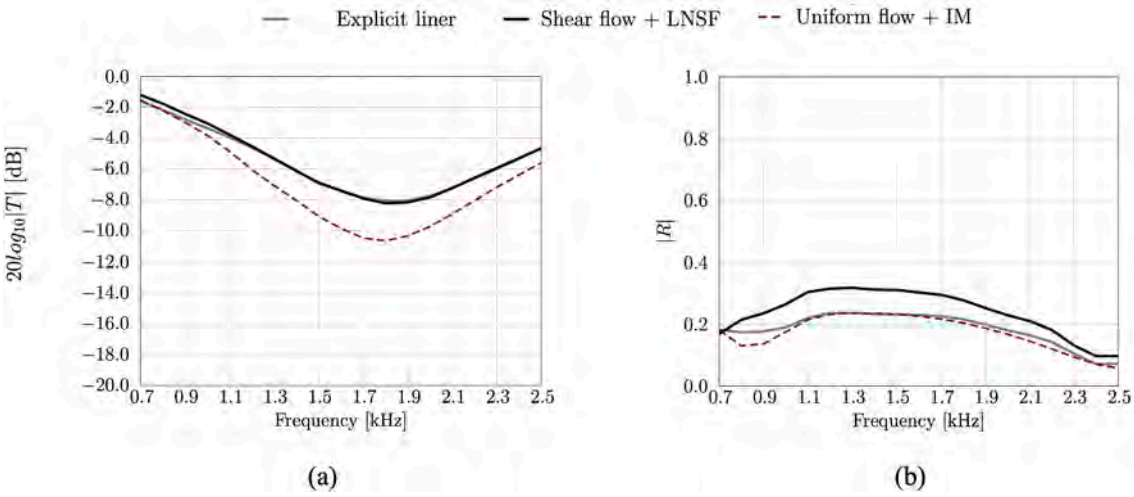


Fig. 8. Transmission (a) and reflection (b) coefficients for the uniform impedance boundary-condition simulations with an upstream acoustic source, compared with the explicit liner simulation.

Following [14,15], the adequacy of the impedance boundary condition is assessed by comparing the transmitted and reflected acoustic waves at the interfaces between the hard-wall and impedance-wall sections.

5.1. Transmission and reflection coefficient

Fig. 8 reports the transmission and reflection coefficients extracted from the scattering matrix [14] for the impedance-boundary configurations and compares them against the explicit liner simulation. All cases are computed at the same SPL and with the same upstream acoustic source location.

Fig. 8(a) shows that all cases are characterised by similar frequency dependence of the transmission coefficient. In particular, the transmission decreases with frequency up to 1800 Hz, where it shows a minimum. Among the simplified models, the configuration sheared flow + LNSF (case II) provides the closest agreement with the explicit liner simulation. By contrast, the uniform-flow model combined with the IM condition shows more pronounced deviations: for the same imposed impedance, it predicts lower transmission across the investigated frequency range, i.e. higher acoustic attenuation, consistent with trends reported in the literature [12]. Regarding the reflection coefficient (Fig. 8(b)), similar considerations can be made, but biases are observed. The sheared-flow

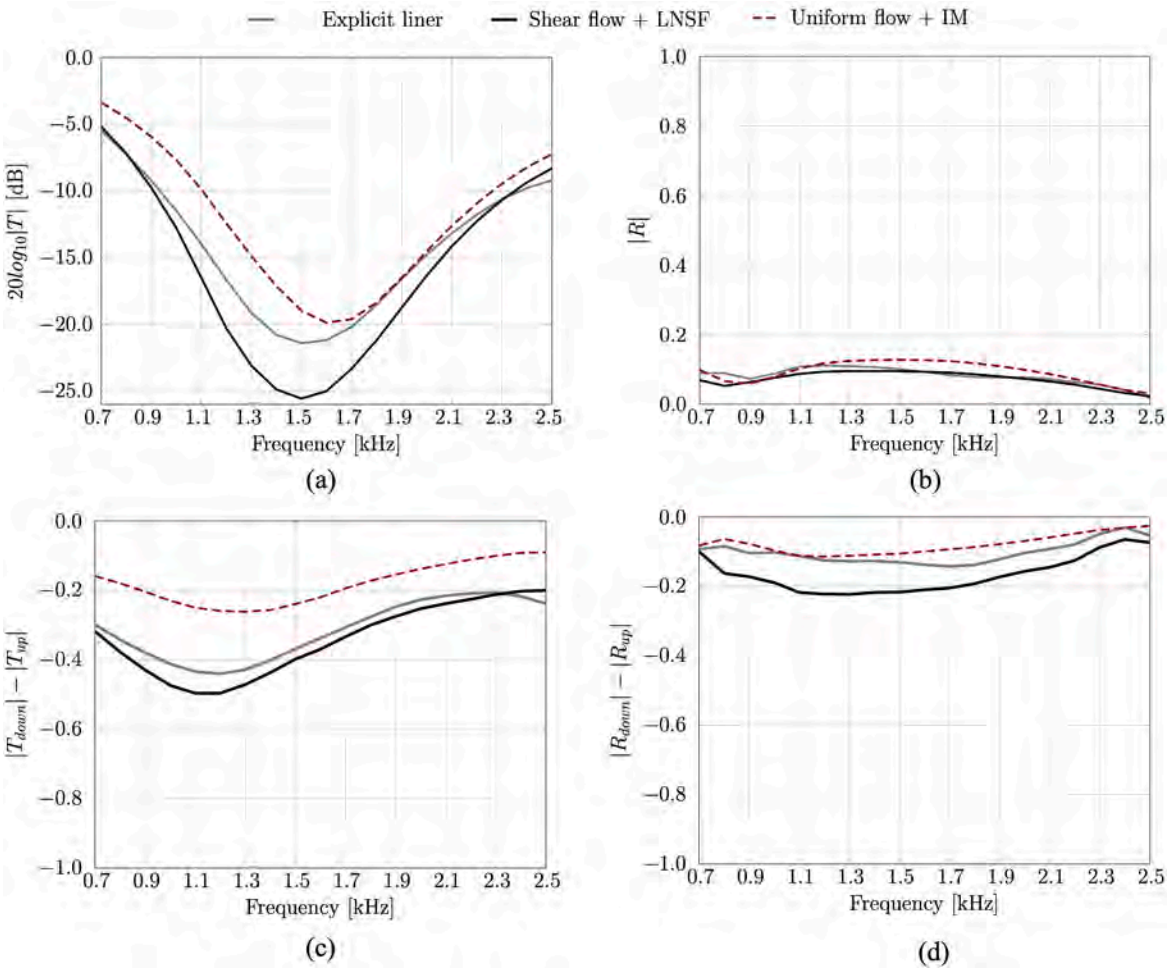


Fig. 9. Transmission (a) and reflection (b) coefficients for the impedance-boundary simulations with a downstream acoustic source; difference in transmission (c) and reflection (d) coefficients compared with the upstream acoustic source, compared with the explicit liner simulation.

LNSF configuration tends to overpredict reflection, whereas the uniform-flow + IM model (case III) yields reduced reflection levels. This difference might arise because the uniform flow assumption does not account explicitly for the shear velocity profile's interaction with incident acoustic waves, thereby suppressing the partial reflections and refractions typically induced by hydrodynamic velocity gradients in the boundary layer. Physically, these near-wall flow gradients cause reflection of incident waves, redistributing acoustic energy across modes and modulating the effective surface impedance. Since models with uniform flow omit this mechanism, they may underpredict the back-reflected energy, which could explain the overestimated attenuation with underestimated reflection for upstream-propagating waves [40].

5.2. *Effect of the acoustic wave propagation direction*

Fig. 9(a,b) report the transmission and reflection coefficients for a downstream acoustic source across all configurations and frequencies at the same SPL. In this set of simulations, the impedance is kept constant in order to enable a direct comparison with the upstream-source cases and to isolate the effect of acoustic-wave propagation direction on the resulting acoustic field. The influence of using different impedance values is further examined in Appendix E.

Compared with the upstream-source configuration, the differences between models are more pronounced. While all cases retain similar trends, the sheared flow + LNSF configuration (case II) predicts lower transmission than the explicit liner simulation, whereas the uniform-flow configuration (case III) predicts higher transmission. In addition, the frequency at which the minimum transmission occurs differs between models: both the explicit liner simulation and the sheared flow + LNSF case exhibit a minimum at 1500 Hz, whereas the uniform-flow case exhibits its minimum at 1600 Hz. The reflection coefficient shows a comparable frequency dependence across cases, with smaller case-dependent variations than those observed for transmission.

Both coefficients vary with source location, in agreement with established findings for lined ducts in the presence of flow [11,40]. For transmission coefficients, all configurations yield reduced values compared with the upstream-source case, and the sheared flow

+ LNSF configuration follows the explicit liner results more closely. The IM-based uniform-flow configuration is shifted toward higher transmission values. For reflection, all cases yield lower reflection when the source is located downstream (i.e. when waves propagate upstream), confirming a marked directional dependence of the scattering response in the presence of mean flow [11,40]. In agreement with previous findings in the literature [12,18], this demonstrates that identical impedance values produce markedly different transmitted and reflected fields based on the acoustic wave propagation direction in the presence of flow. For instance, an incoming plane wave experiences distinct absorption at the liner wall when travelling against the flow. This behaviour might be explained by the competition between convective and refractive effects of the mean flow. Waves travelling against the flow propagate with a lower effective speed and therefore experience a longer interaction with the lined wall, whereas refraction in the sheared boundary layer acts in the opposite direction: rays are pushed towards the regions of low local wave speed; consequently, they are trapped near the wall when propagating downstream and pushed towards the duct's center when propagating upstream [40]. The mean flow breaks the reciprocity relation that holds under zero-flow conditions, yielding asymmetric scattering responses [11]. The present results extend the findings of [12,41] to cases including viscosity and show that the portion of the reflected and transmitted acoustic field, depending on the propagation direction, is sensitive to the model used for the calculation of the acoustic field, even when the impedance wall is kept equal. Fig. 9(c) and (d) quantify the dependence of transmission and reflection on the acoustic propagation direction through the metrics $\Delta T = \left|T_{\text{down}}\right| - \left|T_{\text{up}}\right|$, $\Delta R = |R_{\text{down}}| - |R_{\text{up}}|$, where the superscripts $down$ and up denote downstream- and upstream-source locations, respectively. When the sheared mean-flow profile is accounted for, the resulting direction-dependent variations of the transmission and reflection coefficients for a fixed imposed impedance closely resemble those obtained with the explicit liner configuration.

These results demonstrate that applying identical impedance boundary conditions across different acoustic models yields distinct acoustic fields. Since impedance eduction techniques function by minimising the discrepancy between experimental measurements and a specific numerical prediction, the resulting impedance values are inherently coupled to the selected method. Consequently, the impedance values are quantitatively meaningful only when applied within the same acoustic framework used for their derivation. This dependency challenges the interpretation of acoustic impedance as a unique, model-independent integral parameter.

5.3. Acoustic induced velocity profiles

The differences in the acoustic field are further examined in terms of the amplitude of the wall-normal ($|\tilde{v}|$) and streamwise ($|\tilde{u}|$) acoustic-induced velocities. Since these velocities represent the modal shape of the acoustic field, their variations enable the assessment of the effects of incorporating the shear flow profile and viscous effects on the resulting acoustic response. Fig. 10 displays the amplitude of the acoustic-induced velocity profile for an upstream acoustic source.

For the sake of conciseness, only three representative frequencies are discussed.

The analysis of the wall-normal acoustic-induced velocity shows that cases employing a sheared flow profile exhibit a monotonic increase in velocity amplitude towards the impedance wall, with the most pronounced variations occurring within the region $y/\delta^* < 1$, where δ^* denotes the boundary-layer displacement thickness. This behaviour highlights the role of local velocity gradients in shaping the near-wall acoustic response.

In contrast, when a uniform base flow is assumed, the wall-normal acoustic-induced velocity increases with an approximately constant slope from the channel centre towards the impedance boundary, reflecting the absence of shear-induced modulation. As the frequency increases, the liner reactance increases, resulting in a different wall-normal velocity imposed at the impedance boundary.

The streamwise acoustic-induced velocity similarly exhibits a sharp increase in the near-wall region for all frequencies when a sheared flow is considered. Under uniform flow conditions, however, the streamwise velocity profiles remain nearly uniform across the channel height. A key observation is that the peak amplitude of the streamwise acoustic-induced velocity decreases with increasing frequency. The streamwise velocity does not represent an independent acoustic response, but is generated through the interaction between wall-normal acoustic motion and the base-flow shear via the term $\tilde{v}\,\mathrm{d}U/\mathrm{d}y$ in the linearised momentum equation [13,19]. Nevertheless, the reduction in streamwise velocity amplitude cannot be attributed solely to changes in the wall-normal velocity magnitude. In the frequency-domain formulation, the streamwise momentum equation includes the inertial term $\mathrm{i}\omega\tilde{u}$, which becomes increasingly dominant at higher frequencies. As a result, the response of the streamwise velocity is progressively reduced, limiting the conversion of wall-normal acoustic motion into streamwise fluctuations.

For a downstream acoustic source (Fig. 11), the influence of the base flow beyond the region $y/\delta^* < 1$ is again evident. In this case, however, the wall-normal velocity profiles exhibit an opposite near-wall trend compared to the upstream configuration: the velocity increases monotonically towards the impedance wall before undergoing a sharp reduction within the region $y/\delta^* < 1$.

Finally, it is noted that for all cases considered, the differences between modelling approaches manifest not only in the spatial distribution of the acoustic-induced velocities but also in their absolute values at the wall. This effect is particularly significant for the wall-normal velocity component, which directly reflects the fluctuation imposed by the impedance boundary condition.

6. Impedance eduction

Discrepancies in the acoustic fields and velocity distributions arising from different modelling assumptions can lead to variations in the equivalent impedance obtained with conventional eduction techniques. In this section, the impact of flow modelling on the

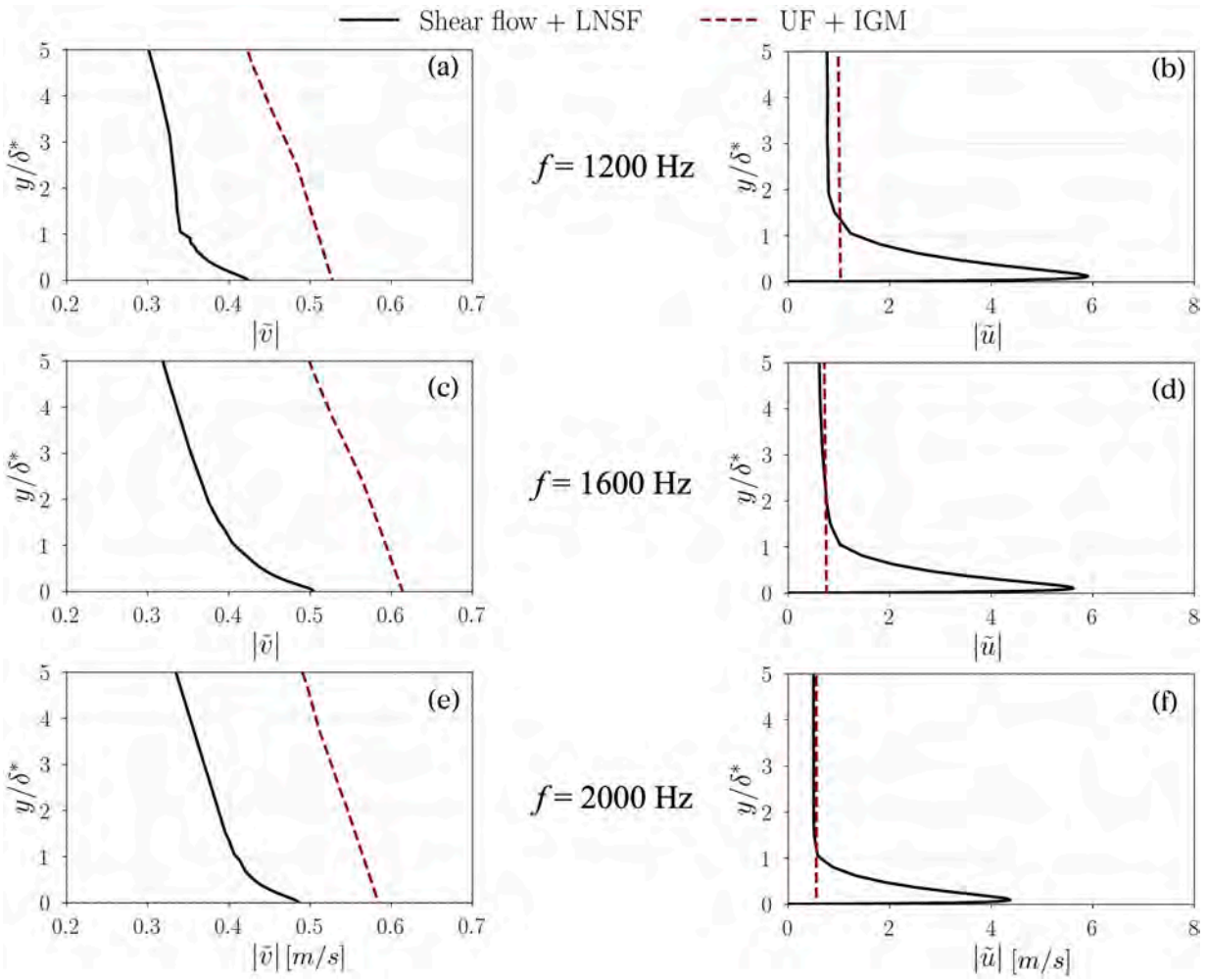


Fig. 10. (a, c, e) Wall-normal acoustic-induced velocity, (b, d, f) streamwise acoustic induced velocities. The velocity profiles for the two cases are compared at three frequencies of interest, considering an acoustic source located upstream of the liner.

educed impedance is investigated by using the flow–acoustic duct models described above as the forward model for impedance eduction.

6.1. Impedance eduction method

The method begins with complex acoustic pressures sampled at multiple streamwise locations, either in experiments or in simulations. These data are recast into a set of complex transfer functions constructed from the microphone signals. For each microphone n, the transfer function is defined relative to a reference microphone (labelled 1) as:

$$H_{r,n}(\omega) = \frac{\tilde{p}_{t_n}(\omega)}{\tilde{p}_{t_1}(\omega)}, \tag{21}$$

where $\tilde{p}_{t_n}(\omega)$ and $\tilde{p}_{t_1}(\omega)$ denote the complex acoustic pressures measured at the nth microphone and at the reference microphone, respectively. A schematic representation of the number and location of microphones is reported in Fig. 12. The reference microphone is selected on the source side: for an upstream source, it is the most upstream microphone, whereas for a downstream source, it is the most downstream microphone (i.e., closest to the source). This choice ensures that all transfer functions are defined consistently with the measurement configuration.

For a given trial impedance, the forward prediction is obtained through the FEM solver. First, the flow profile is obtained by performing a RANS simulation of the duct with smooth walls to reproduce the mean-flow conditions. Then, the LNSF equations are solved on the same geometry with the liner represented by an impedance boundary condition. The resulting complex pressure field is sampled at the microphone locations and used to compute the model transfer functions, $H_{lm,n}(\omega)$, using the same definition as for the

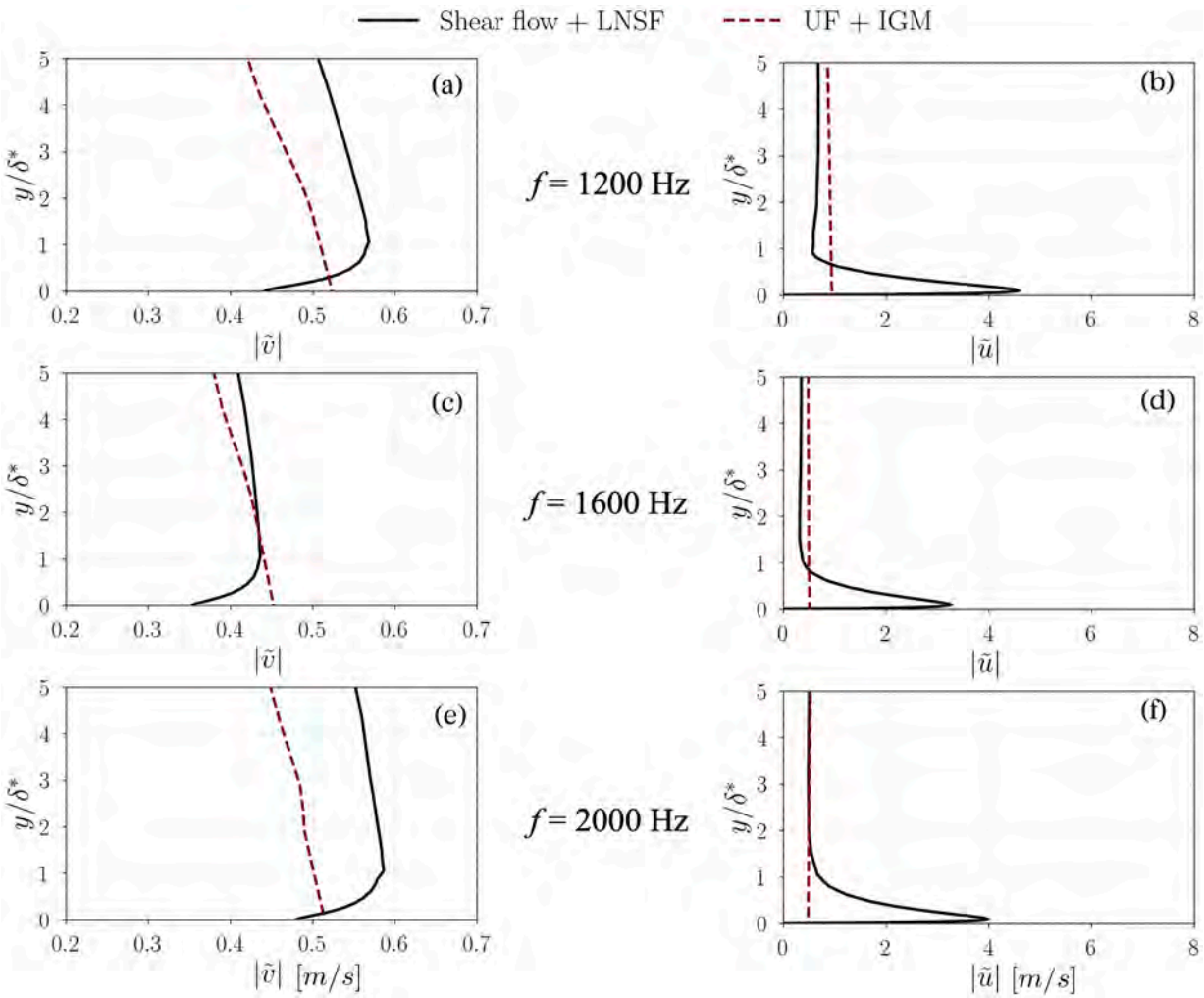


Fig. 11. (a, c, e) Wall-normal acoustic-induced velocities, (b, d, f) streamwise acoustic induced velocities. The velocity profiles for the two cases are compared at three frequencies of interest, considering an acoustic source located downstream of the liner.

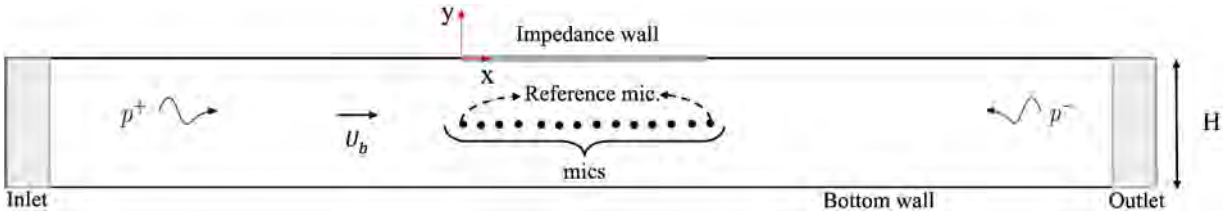


Fig. 12. Schematic representation of the number and locations of microphones used for acquiring pressure measurements.

reference data (Eq. (21)). The impedance is identified by minimising the mismatch between reference and model transfer functions across the microphone array. The residual at a given frequency is defined as the sum of squared differences in real and imaginary parts:

$$\text{Res} = \sum_{n=1}^{N_{mic}} \left(\Re\left[H_{r,n}(\omega) - H_{lm,n}(\omega)\right]\right)^2 + \left(\Im\left[H_{r,n}(\omega) - H_{lm,n}(\omega)\right]\right)^2, \tag{22}$$

where N_{mic} is the total number of microphones, and $\Re(\cdot)$ and $\Im(\cdot)$ denote the real and imaginary parts, respectively. This formulation avoids weighting ambiguities between magnitude and phase and provides a single scalar measure of agreement between the measured and modelled transfer functions. The eduction is performed independently at each frequency.

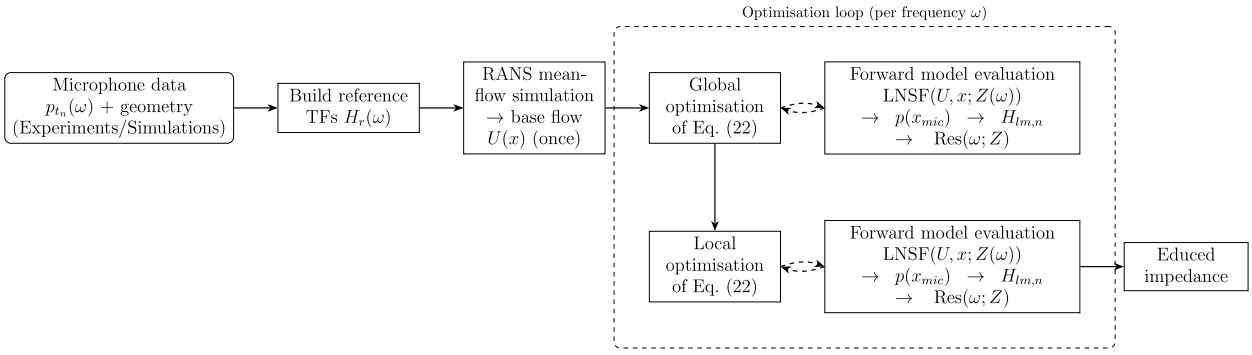


Fig. 13. Sketch of the impedance eduction technique.

6.1.1. Hybrid optimisation procedure

To mitigate bias from initial conditions and avoid entrapment in local minima, a two-step hybrid optimisation strategy is employed. The global optimisation is performed using the deterministic DIRECT algorithm [42], which systematically partitions the search space to efficiently explore multiple local minima, enhancing convergence robustness [42]. In this first part of the optimisation process, the initial search is constrained to $\theta \in [0.01, 4]$ and the reactance to $\chi \in [-4, 4]$. The lower bound on the resistance ($\theta > 0$) enforces a passive impedance throughout the search, so that active solutions are excluded by construction. The global optimisation phase is considered converged once the error falls below a predefined threshold ($1 \cdot 10^{-4}$) or the maximum number of iterations is reached (200 iterations is set as the maximum for this step). The results from this phase serve as the initial guess for the subsequent local optimisation, which employs a simplex-based method following the approach of [43] for impedance eduction. Specifically, a variant of the Nelder-Mead simplex algorithm called SUBPLEX [44] is used. SUBPLEX is a derivative-free local optimiser that recursively performs simplex optimisations within subspaces of the overall parameter space, enabling effective convergence even in complex or noisy objective landscapes. Convergence for the local phase is declared when the error reduces below a chosen threshold ($1 \cdot 10^{-6}$ in the present approach) or the maximum number of iterations is reached (in the present approach 200 iterations is set as the maximum for this step).

The combination of DIRECT for global search and SUBPLEX for local tuning offers a balanced approach, providing broad domain coverage alongside precise convergence to the optimal liner impedance. Fig. 13 illustrates the workflow of the eduction technique, outlining the sequence from data acquisition to impedance identification and G shows the residual landscape for a reference frequency to investigate the uniqueness and robustness of the educed impedance.

6.2. Impedance eduction results

Fig. 14 presents the impedance results obtained using the eduction procedure detailed in Section 6 for the acoustic model considering the sheared flow + LNSF. Panels (a) and (b) show the resistance and reactance values obtained with the fully resolved sheared flow profile coupled with the LNSF framework compared with the impedance educed with the MM technique, i.e. uniform flow assumption + IM boundary condition, applied to the same acoustic field. Panels (c) and (d) report the absolute differences in resistance, $|\Delta\theta| = ||\theta_{\text{down}}| - |\theta_{\text{up}}||$, and reactance, $|\Delta\chi| = ||\chi_{\text{down}}| - |\chi_{\text{up}}||$.

The proposed eduction technique yields resistance values that decrease in magnitude with frequency and reactance values that increase accordingly, consistent with Fig. 5. A notable observation emerges from comparing impedance values between downstream and upstream configurations: while the downstream source produces slightly higher resistance and marginally different reactance, the differences between upstream and downstream are lower with respect to those obtained using the MM method. At low frequencies, the resistance is nearly identical, with the maximum deviation occurring at $f = 1300$ Hz where $|\Delta\theta| = 0.18$. The two curves tend to converge at higher frequencies, consistent with experimental and numerical studies of impedance eduction performed with inverse techniques [36,45,46]. The reactance exhibits variations at the lowest frequencies, which may be attributed to the limited length of the tested liner sample.

Taken together, Fig. 14(c) and (d) show that the present eduction procedure substantially reduces—though does not eliminate—the propagation-direction dependence of the educed impedance. This reduction is an important outcome of the study: when the eduction technique includes both the sheared flow and viscous acoustic effects, the resulting educed impedance becomes markedly less sensitive to source location than typically reported when other acoustic models are used [36,45,46]. A residual difference between propagation directions nevertheless persists and is examined below using field-level quantities. This result is in agreement with what was found by Paduano et al. [5] using the in-situ technique, where no assumptions on the flow are made.

Fig. 15 reports contours of the wall-normal, acoustically induced velocity magnitude ($|\tilde{v}|$) above (i) the explicit liner and (ii) the equivalent impedance boundary condition for the sheared flow + LNSF case, for both upstream- and downstream-source configurations. The excitation frequency is fixed at 1300 Hz, and the imposed impedance boundary conditions use the values educed at this frequency (Fig. 14) for the corresponding source location (Panels (b) and (d)). This frequency is selected because it yields the largest difference between the upstream- and downstream-educed impedances.

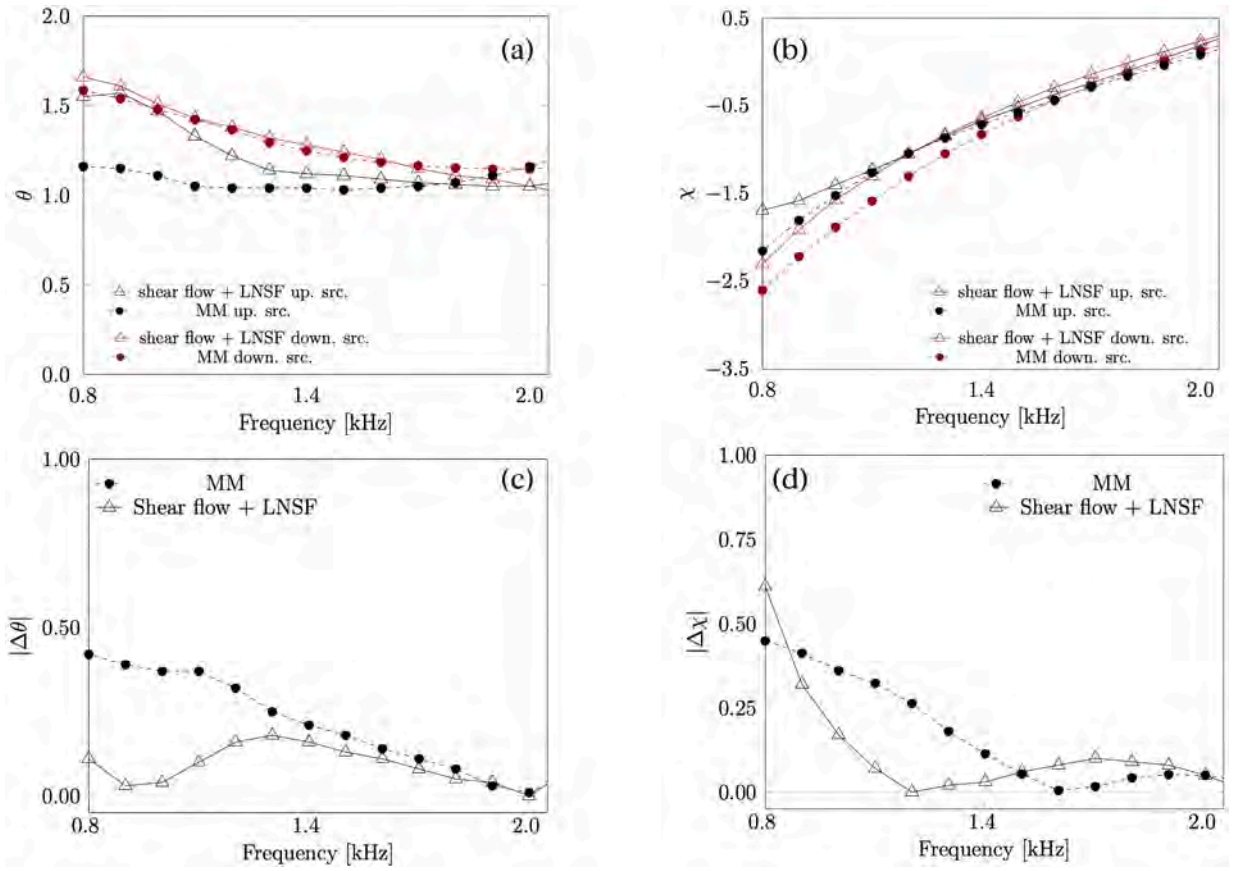


Fig. 14. Resistance (a) and Reactance (b) educed with the sheared flow + LNSF approach for two different acoustic wave propagation directions. Differences in resistance (c) $|\Delta\theta| = ||\theta_{\text{down}}| - |\theta_{\text{up}}||$ and (d) $|\Delta\chi| = ||\chi_{\text{down}}| - |\chi_{\text{up}}||$ for different eduction methods. The SPL is fixed for all cases and set equal to 145 dB.

Two features are apparent. First, the magnitude of the acoustic-induced velocity above the impedance boundary is up to five times lower than that observed above the explicit liner, as can be noted by comparing the colour maps. This reduction might be attributed to the assumption of a uniform impedance wall, which leads to a more spatially distributed velocity fluctuation compared to the explicit liner, where fluctuations are concentrated within the orifices. Second, the spatial distribution differs between the two cases. In the explicit liner case, the largest velocities are localized over the liner, and the peak magnitude does not change substantially between upstream and downstream excitation. In the impedance-boundary case, peaks in $|\tilde{v}|$ appear near the two ends of the impedance patch for both source locations, consistent with the abrupt impedance discontinuity at the hard/impedance interfaces [21]. Differences between upstream and downstream excitation are more pronounced in the impedance-boundary case, particularly near the downstream interface.

These differences might provide useful context for interpreting residual directionality in the educed impedance. In the imposed-impedance simulations, the mean-flow profile above the impedance wall does not reproduce the near-wall velocity deficit observed at the downstream end of the explicit liner simulation (Fig. 7). Consequently, even though the acoustic equations account for shear and viscosity, the base-flow environment in which the impedance boundary is applied differs from that of the explicit liner case. In addition, the transmitted/reflected fields at the hard/impedance interfaces depend on propagation direction in the presence of shear flow [40]. In this context, the eduction procedure yields an equivalent impedance that matches the measured transfer functions within the adopted eduction technique and mean-flow representation. A physically consistent way to recover the missing near-wall velocity deficit would be to reproduce the orifice-induced momentum exchange through an equivalent roughness or transpiration boundary condition applied to the mean flow. In this respect, impedance-type wall conditions for the fluid-dynamic field, forced by the pressure content of the turbulent boundary layer [32], could serve as such a transpiration condition; this development is, however, beyond the scope of the present study.

To further assess the significance of the remaining impedance differences, an additional test is performed at $f = 1300$ Hz. The two impedance values educed from the upstream- and downstream-source configurations are separately imposed as boundary conditions while keeping the acoustic source upstream (SPL = 145 dB). The resulting transfer functions from the sheared flow and LNSF case are compared with the explicit liner reference. Fig. 16 shows the amplitude and phase of the transfer function defined in

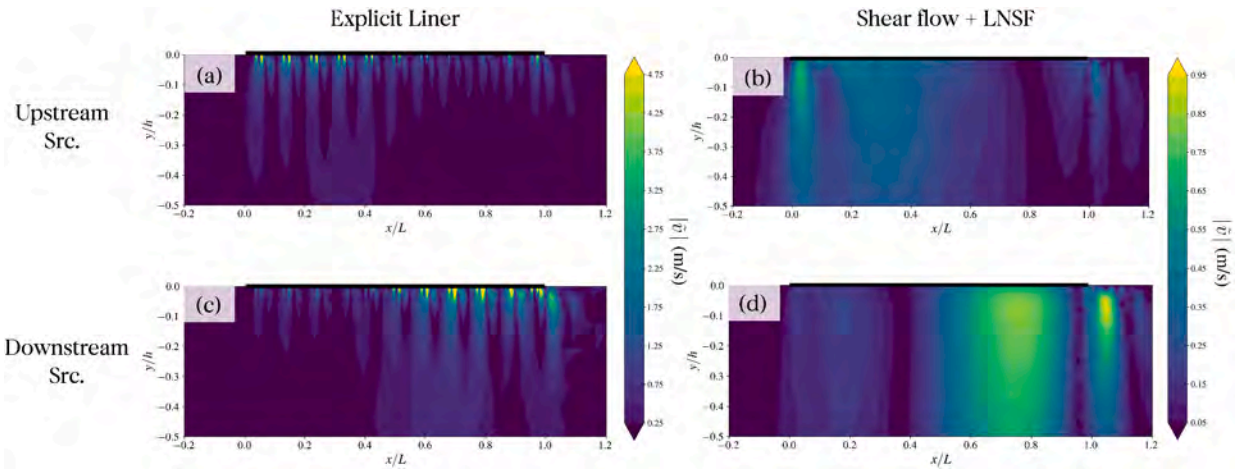


Fig. 15. The $|\bar{v}|$ field in the $x-y$ plane above the liner (a, c) and the impedance boundary condition (b, d) (note the change in velocity scales between the figures). Upstream acoustic source (a, b), downstream acoustic source (c, d). All cases present SPL equal to 145 dB and $f = 1300$ Hz and $U_b = 100\,\mathrm{m\,s^{-1}}$.

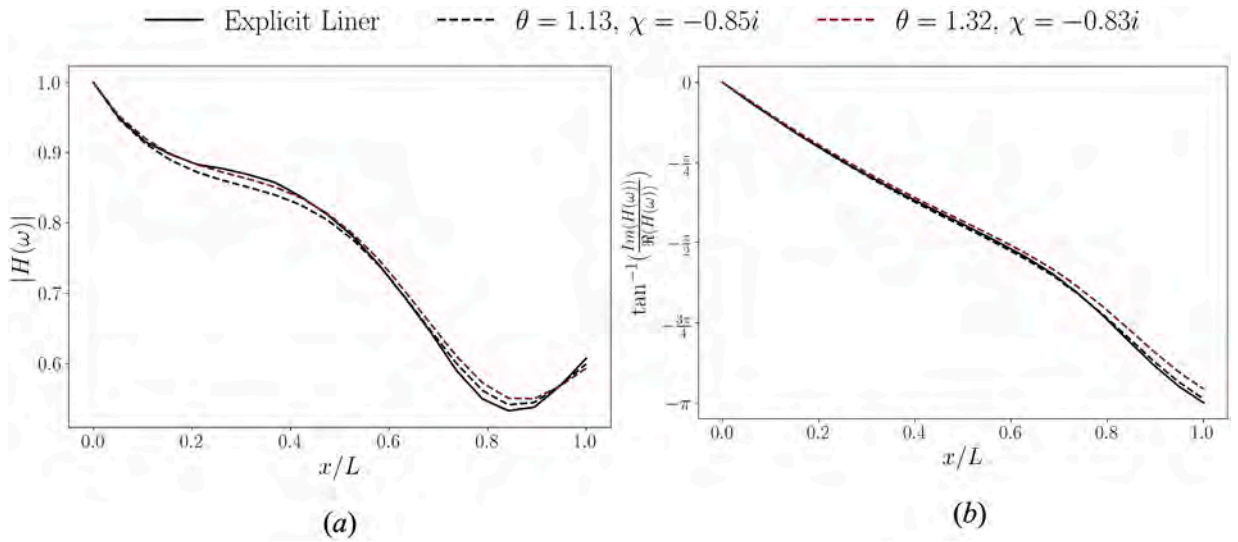


Fig. 16. Transfer function amplitude (a) and phase (b) of the explicit liner compared with impedance boundary conditions of $\theta = 1.13$, $\chi = -0.85$ and $\theta = 1.32$, $\chi = -0.83$. In all cases, the acoustic source is located upstream of the liner and has an SPL of 145 dB at $f = 1300$ Hz and the bulk velocity is $U_b = 100\,\mathrm{m\,s^{-1}}$.

Eq. (21). The two imposed impedance values lead to distinct transfer functions, demonstrating that the residual differences between the educed impedance values correspond to measurable differences in the predicted acoustic field. When the impedance educed from the downstream-source case is applied, the mismatch with respect to the explicit liner reference increases, with the residual (Eq. (22)) rising from 5.3×10^{-3} to 3.37×10^{-2}.

However, it is worth noting that even the upstream-source educed impedance does not perfectly reproduce the explicit liner transfer function. This indicates that, within the present modelling framework, discrepancies remain between the explicit liner and the uniform impedance-wall representation. In particular, the imposed boundary condition models the liner as spatially uniform, and the mean-flow profile applied in the eduction model does not include the streamwise modifications associated with the explicit liner geometry. These aspects are not represented in the current impedance-boundary formulation and are therefore reflected in the residual differences observed in Fig. 16.

7. Conclusions

This study introduces and adopts a mid-fidelity numerical framework that couples Reynolds-averaged Navier–Stokes (RANS) simulations of the mean flow with frequency-domain aeroacoustic analyses to assess the effect of the flow and acoustic field modelling

on educed impedance. First, the approach is validated against high-fidelity numerical simulations and experimental data and then applied within the scope of the study. The results demonstrate that the framework, when applied to the three-dimensional liner geometry, well reproduces the streamwise development of the flow and effectively captures the multi-frequency behaviour of the acoustic liner in terms of impedance, including its dependence on acoustic wave propagation direction. Quantitatively, the framework reproduces the experimental resistance with a mean absolute error of 0.27 (upstream source) and 0.36 (downstream source), and the reactance with a mean absolute error of 0.09 and 0.07, respectively. The residual resistance gap is shown to be consistent with the high-SPL nonlinear orifice contribution, which is intrinsically absent from the linear formulation, as estimated through the semi-empirical model of Yu et al. [34].

Based on the results of the explicit liner simulation, frequency-dependent impedance boundary conditions have been tested across different base flow and acoustic modelling scenarios, revealing important insights into their practical applicability. The findings emphasise the necessity of using impedance as a boundary condition consistent with the acoustic and flow framework from which it was derived. When the same impedance value is used, but the presence of a shear flow profile is omitted, a different acoustic field and acoustic-induced velocity over the boundary condition are obtained compared to cases where both the base shear flow profile and viscous effects are accounted for. This is attributed to the fact that introducing a shear base flow results in non-reciprocity of the reflection coefficient depending on acoustic wave propagation direction.

Building on these findings, an impedance eduction methodology was developed, leveraging a finite element framework combined with a dual step optimisation algorithm. This approach uses a shear base flow profile and accounts for the acoustic viscous boundary layer, yielding educed impedance values with reduced directional dependence ($\theta_{down} - \theta_{up} \approx 0.18$) relative to previously reported methods in the literature ($\theta_{down} - \theta_{up} \approx 0.40$). This might indicate that, for the present liner impedance and flow condition, some of the formerly observed large discrepancies can be attributed to modelling simplifications.

Nonetheless, despite these improvements, a residual dependence of the educed impedance on the direction of acoustic wave propagation persists. It is important to highlight that the current eduction framework, despite incorporating the shear base flow profile and acoustic viscous boundary layer, retains key limitations stemming from its representation of the acoustic liner as a uniform, smooth surface with prescribed impedance. This simplification neglects the inherent surface roughness of actual liners, yielding two principal shortcomings: it (i) alters the downstream shear profile evolution relative to smooth-wall assumptions, influencing directional reflectivity, and (ii) yields mismatched acoustic-induced velocity distributions versus explicit liner cases. Addressing this shortcoming represents a promising path for future research aimed at improving the predictive fidelity and broader applicability of impedance eduction methodologies. This could include an impedance boundary condition for the fluid dynamic field, which also accounts for velocity in the wall-normal direction, potentially leading to a more representative evolution of the near-wall flow.

Overall, this work advances the understanding of liner impedance characterisation, providing a validated, computationally efficient framework that bridges flow physics and practical acoustic modelling for improved design and analysis of acoustic liners in aeroacoustic applications.

CRediT authorship contribution statement

Angelo Paduano: Writing – review & editing, Writing – original draft, Validation, Methodology, Investigation, Formal analysis, Conceptualization; **Francesco Scarano:** Writing – review & editing, Investigation; **Lucas A. Bonomo:** Writing – review & editing; **Damiano Casalino:** Writing – review & editing, Supervision, Methodology; **Julio A. Cordioli:** Writing – review & editing, Supervision; **Francesco Avallone:** Writing – review & editing, Supervision, Investigation, Conceptualization, Funding acquisition.

Declaration of competing interest

The authors declare that they have no known competing financial interests or personal relationships that could have appeared to influence the work reported in this paper.

Acknowledgments

The work of A. Paduano, F. Scarano and F. Avallone is co-funded by the European Union (ERC, LINING, 101075903). Views and opinions expressed are, however, those of the author(s) only and do not necessarily reflect those of the European Union or the European Research Council. Neither the European Union nor the granting authority can be held responsible for them. J. A. Cordioli acknowledges funding from the Brazilian funding agency CNPq (National Council for Scientific and Technological Development) through the process 315000/2021-0.

Data availability

Data will be made available on request.

Appendix A. Mesh convergence

The mesh is composed of unstructured tetrahedral cells with prism layers adjacent to the walls. Three mesh resolutions were systematically evaluated to ensure grid independence: medium, fine, and very fine. The results obtained from each configuration

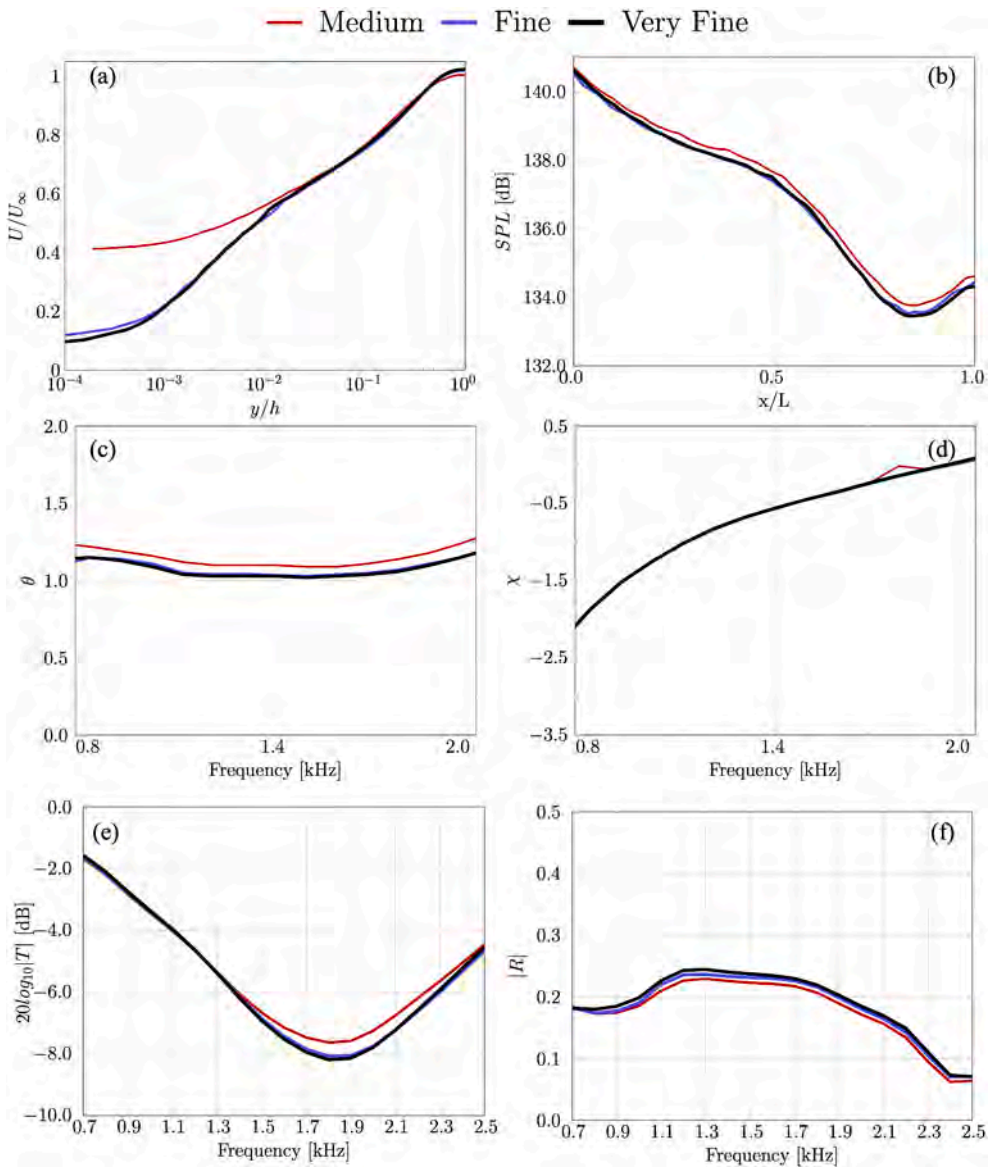


Fig. A.17. Grid-convergence study for the explicitly resolved liner: sheared velocity profile at the liner leading edge (a), SPL decay at 1400 Hz (b) educed resistance θ (c) and reactance χ (d), and transmission (e) and reflection (f) coefficients, for three mesh resolutions.

were compared in terms of the mean streamwise velocity profile at the onset of the liner; the comparison is reported in Fig. A.17(a). As can be clearly seen from the plot, the medium simulation shows a large variation in the velocity profile shape when compared with the fine and very fine simulations, especially near the wall, where the velocity profile is largely overestimated. Moving from the fine to very fine simulations leads to negligible differences in the flow profile at the beginning of the liner.

The mesh convergence study is also performed in terms of acoustic quantities. The grid independence of the results is quantified in terms of SPL decay in Fig. A.17b, resistance and reactance A.17 (c, d) and transmission and reflection coefficient (e, f).

From Fig. A.17, it can be seen that the SPL decay, despite showing variations, is less sensitive to the acoustic mesh refinement. However, the fine and very fine resolutions showed negligible variations in both SPL decay and educed impedance results. Moreover, between the fine and very fine resolutions, the educed resistance and reactance present mean deviations of 0.009 and 0.017, respectively, over the full frequency range, while the transmission coefficient differs by less than 0.12 dB and the reflection coefficient by less than 0.009. By contrast, the medium resolution deviates from the very fine one by up to 0.15 in resistance (mean 0.09) and up to 0.6 dB in transmission. Extended details on the mesh are reported in Table A.2.

Moreover, since the paper also presents the near-wall velocity profiles for the cases with the impedance boundary condition, a separate mesh-convergence study was performed on those simulations; the results are reported in Fig. A.18. The velocity was sampled at the onset of the impedance patch for the case at $f = 2500$ Hz employing sheared flow + LNSF, which is expected to be the most

Table A.2
Mesh parameters for the grid-convergence study. The acoustic viscous boundary-layer thickness $\delta_v = \sqrt{2\nu/\omega}$ and the elements-per-wavelength count are evaluated at the highest frequency considered ($f = 2500$ Hz).

	Medium	Fine	Very Fine
DOF, acoustic solution	$\approx 4.2 \times 10^6$	$\approx 8 \times 10^6$	$\approx 11 \times 10^6$
Elements within δ_v	≈ 5	≈ 10	≈ 15
Elements per orifice diameter	≈ 20	≈ 30	≈ 40
Minimum elements per wavelength λ	8	22	45

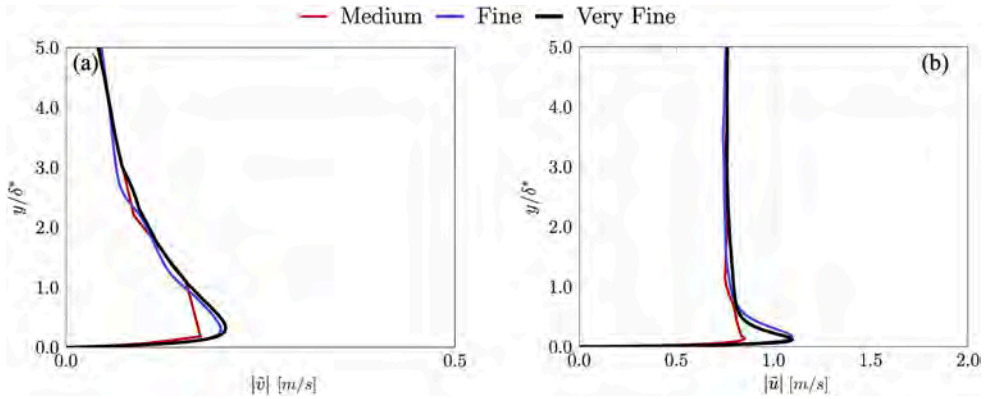


Fig. A.18. Mesh-convergence study for the impedance-boundary-condition simulations with a forcing frequency of $f = 2500$ Hz: wall-normal ($\tilde{v}$) and streamwise ($\tilde{u}$) near-wall velocity profiles at the onset of the impedance patch, for three mesh resolutions.

demanding, as the streamwise velocity components must vanish at the wall and the near-wall gradients are steepest at the highest frequency. As shown in the figure, the medium resolution fails to resolve the near-wall gradients, drastically underestimating the peak of both velocity components, whereas the fine resolution yields streamwise ($\tilde{u}$) and wall-normal ($\tilde{v}$) velocity profiles in good agreement with the very fine simulation, confirming the robustness of the results with respect to mesh refinement.

Appendix B. Estimation of the nonlinear orifice resistance

To quantify the contribution of the high-SPL nonlinear orifice losses, which are intrinsically absent from the present linear formulation, the semi-empirical perforate impedance model of Yu et al. [34] is employed. In this model, the normalised resistance of a perforate facesheet is decomposed into a linear, a grazing-flow and a high-SPL nonlinear contribution:

$$\theta = \theta_o + \theta_{of} + S_r V_p + \theta_{cm}, \tag{B.1}$$

where θ_o is the linear viscous resistance, θ_{of} is the liner frequency-dependent contribution, θ_{cm} is the grazing flow contribution, and $S_r V_p$ the nonlinear term driven by the acoustic particle velocity. The nonlinear slope S_r depends only on the facesheet geometry:

$$S_r = \frac{1.334\left(1-\sigma^2\right)}{2\,C_d^2\,\sigma^2\,c_0}, \tag{B.2}$$

where σ is the facesheet open-area ratio, C_d a discharge coefficient obtained from a geometry-based correlation, and c_0 the speed of sound. The root-mean-square acoustic particle velocity in the orifice, V_p, is solved self-consistently with the imposed SPL and the predicted impedance. The model is evaluated with the open-area ratio of the present liner sample and the boundary-layer displacement thickness obtained from the RANS solution, for the upstream-source configuration at SPL = 145 dB, for which the model is calibrated.

Fig. B.19 compares the educed resistance from the experiments [9], the present RANS–LNSF framework and the model of Yu et al. [34] (a), together with the nonlinear contribution $S_r V_p$ against the resistance gap $\theta_{\text{exp}} - \theta_{sim}$ (b). Two observations follow. First, the semi-empirical model reproduces the experimental resistance with good agreement, especially at high frequencies. Second, and most relevant to the present discussion, the nonlinear SPL-driven term $S_r V_p$ closely matches the gap between the experimental and the computed resistance in both magnitude (mean ≈ 0.23) and frequency trend. This indicates that the systematic resistance underestimation of the present framework is compatible with the neglected high-SPL nonlinear orifice contribution, rather than with an absence of turbulence–acoustic damping, which is accounted for through the eddy viscosity (Section 2.1).

For the downstream-source configuration, no semi-empirical model accounting for the source location is available, and a direct comparison analogous to the upstream case is therefore not possible. Nevertheless, the downstream resistance gap (mean ≈ 0.36) exhibits the same nearly constant, frequency-preserving character, suggesting a common physical origin. Since the neglected losses stem from the acoustic–vortex interaction at the orifices, whose intensity depends on the propagation direction relative to the grazing

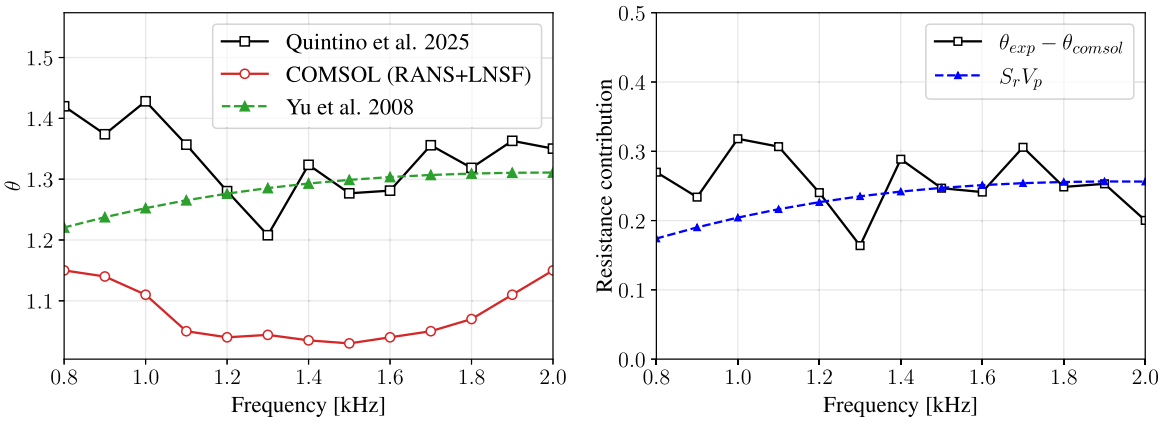


Fig. B.19. (a) Educed resistance from the experiments of Quintino et al. [9], the present framework and the semi-empirical model of Yu et al. [34]; (b) nonlinear SPL-driven contribution $S_r V_p$ compared with the resistance gap $\theta_{\text{exp}} - \theta_{sim}$. Upstream acoustic source, SPL = 145 dB.

flow [5], a larger unrepresented nonlinear contribution in this configuration is plausible, although it cannot be verified with existing semi-empirical models.

Appendix C. Scattering matrix

In this work, the computation of the scattering matrix assumes that only plane waves propagate within the hard-wall sections of the duct. This assumption is not overly restrictive given the present computational setup. The acoustic pressure inside the channel can be expressed as the superposition of upstream- and downstream-propagating plane waves, written as

$$\tilde{p}(x) = A_1^+ \mathrm{e}^{-\mathrm{i}k^+(x-x_{\text{ref}})} + A_1^- \mathrm{e}^{-\mathrm{i}k^-(x-x_{\text{ref}})}, \tag{C.1}$$

where A_1^+ and A_1^- denote the complex amplitudes of the downstream and upstream travelling acoustic waves, respectively. The complex wave numbers associated with these waves are k^+ and k^-, and x_{ref} is an arbitrary reference position within the channel.

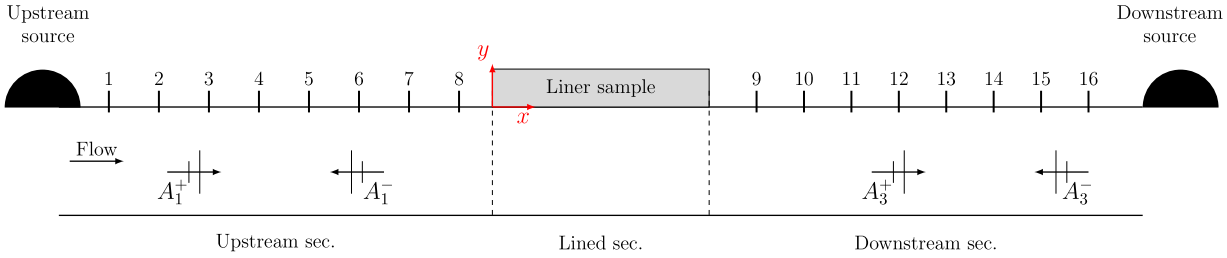


Fig. C.20. Schematic of the overdetermined plane wave decomposition.

To estimate the amplitudes A_1^+ and A_1^-, pressure measurements are collected at multiple microphone locations, with at least three microphones required to yield an overdetermined system. Considering the schematic and notation in Fig. C.20, A_1^+ corresponds to the amplitude of the wave excited by the upstream acoustic source, while A_1^- represents the amplitude of the wave scattered at the liner edges. Similarly, A_3^+ and A_3^- denote the amplitudes of the wave transmitted through the lined section and the wave reflected at the duct termination, respectively.

In the present numerical setup, PMLs are employed to absorb outgoing waves. Consequently, for the upstream source case, A_3^- is assumed to be zero, while for the downstream source case, A_1^+ is set to zero. Previous studies [47] have verified that these assumptions do not compromise the accuracy of the scattering matrix calculation, which is further motivated by the low energy reflected by the PMLs ($< 0.3\%$ of the incident wave).

Using pressure data from the upstream microphones, the amplitudes A_1^+ and A_1^- are computed by solving the following system in a least-squares sense:

$$\begin{bmatrix} \mathrm{e}^{-\mathrm{i}k^+x_1} & \mathrm{e}^{-\mathrm{i}k^-x_1} \\ \mathrm{e}^{-\mathrm{i}k^+x_2} & \mathrm{e}^{-\mathrm{i}k^-x_2} \\ \mathrm{e}^{-\mathrm{i}k^+x_3} & \mathrm{e}^{-\mathrm{i}k^-x_3} \\ \vdots & \vdots \\ \mathrm{e}^{-\mathrm{i}k^+x_8} & \mathrm{e}^{-\mathrm{i}k^-x_8} \end{bmatrix} \begin{bmatrix} A_1^+ \\ A_1^- \end{bmatrix} = \begin{bmatrix} \tilde{p}_1 \\ \tilde{p}_2 \\ \tilde{p}_3 \\ \vdots \\ \tilde{p}_8 \end{bmatrix}. \tag{C.2}$$

Table C.3
Condition number of the microphone-array least-squares system as a function of frequency.

frequency [Hz]	700	800	900	1000	1100	1200	1300	1400	1500	1600	1700	1800	1900	2000	2100	2200	2300	2400	2500
$\kappa(A)$	2.38	2.06	1.81	1.62	1.45	1.32	1.21	1.11	1.03	1.03	1.09	1.14	1.19	1.22	1.25	1.26	1.26	1.24	1.22

The scattering matrix $\mathbf{S}$ relates the transmitted and reflected wave amplitudes to the incident ones through

$$\begin{bmatrix} A_3^+ \\ A_1^- \end{bmatrix} = \mathbf{S} \begin{bmatrix} A_1^+ \\ A_3^- \end{bmatrix} = \begin{bmatrix} T^+ & R^- \\ R^+ & T^- \end{bmatrix} \begin{bmatrix} A_1^+ \\ A_3^- \end{bmatrix}, \tag{C.3}$$

where T and R denote the transmission and reflection coefficients, respectively, defined as

$$T^+ = \frac{A_3^+}{A_1^+}, \quad R^+ = \frac{A_1^-}{A_1^+}, \quad T^- = \frac{A_1^-}{A_3^-}, \quad R^- = \frac{A_3^+}{A_3^-}. \tag{C.4}$$

The plane-wave assumption adopted in the scattering-matrix computation is justified by verifying that the first higher-order transverse modes remain cut-off over the entire frequency range investigated. For a rectangular duct carrying a uniform axial flow at Mach number M_b, the cut-on frequency of the (m, n) transverse mode is [48,49]

$$f_{c,(m,n)} = \frac{c_0}{2} \sqrt{1 - M_b^2} \sqrt{\left(\frac{m}{L_y}\right)^2 + \left(\frac{n}{L_z}\right)^2}, \tag{C.5}$$

where $L_y = H$ and L_z are the wall-normal and spanwise duct dimensions, respectively, and the factor $\sqrt{1 - M_b^2}$ accounts for the convective effect of the mean flow, which lowers the cut-on frequency relative to the no-flow case. Using the bulk Mach number $M_b = 0.296$ as a uniform-flow approximation, together with $H = 40$ mm and $L_z = 12.44$ mm, the first wall-normal mode cuts on at $f_{c,(1,0)} \approx 4.1$ kHz, while the first spanwise mode cuts on at $f_{c,(0,1)} = 26$ kHz. The high cut-on frequency is explained by the fact that the periodic boundary conditions are applied in the spanwise direction, so that the first non-planar spanwise mode has wavenumber $2\pi/L_z$ rather than π/L_z. Both values lie well above the maximum frequency considered in this work (2.5 kHz), confirming that only plane waves propagate in the hard-wall sections of the duct and that the plane-wave decomposition underlying the scattering-matrix formulation is appropriate. We note that Eq. (C.5) assumes a uniform mean flow; the large margin between the lowest cut-on frequency and the analysed range makes this approximation inconsequential for the present assessment.

C.0.0.1. Conditioning of the decomposition. The robustness of the wave decomposition to perturbations in the measured pressures is characterised through the condition number of the decomposition matrix A, defined via its singular value decomposition as $\kappa(A) = \sigma_{\max}(A)/\sigma_{\min}(A)$. For the least-squares system $A\mathbf{x} = \mathbf{b}$, where $\mathbf{x}$ collects the wave amplitudes and $\mathbf{b}$ the microphone pressures, the relative error on the solution is bounded by [50]

$$\frac{\|\delta\mathbf{x}\|}{\|\mathbf{x}\|} \leq \kappa(A) \frac{\|\delta\mathbf{b}\|}{\|\mathbf{b}\|}, \tag{C.6}$$

so that $\kappa(A)$ directly quantifies the amplification of input errors. The condition number does not exceed 2.38 across the entire frequency range (Table C.3), so that input perturbations are amplified by at most a factor of about 2.4, indicating a well-posed decomposition. The maximum occurs at the lowest frequency, where the acoustic wavelength is largest relative to the microphone spacing, while the array is best conditioned ($\kappa \approx 1$) around the centre of the range. Ill-conditioning would correspond to $\sigma_{\min} \to 0$, which physically occurs at the degenerate frequencies where the microphone spacing approaches a half-wavelength [51,52]; the microphone arrangement employed avoids these frequencies over the entire range. The relative least-squares residual of the decomposition remains small (below 3.5×10^{-2}), confirming both that the hard-wall field is well represented by two plane waves and that the second-order term in κ^2 in the perturbation bound is negligible [50].

Appendix D. Isolation of viscous effects: sheared flow with inviscid acoustics

The comparison presented in Section 5 involves two propagation models that differ simultaneously in the base-flow representation (sheared versus uniform) and in the acoustic formulation (viscous versus inviscid). To isolate the specific contribution of the acoustic viscous effects, an intermediate configuration is considered here, in which the sheared mean-flow profile of case II is retained while the acoustic field is solved with the Linearised Euler Equations (LEE) in the frequency domain, i.e. neglecting the viscous and thermal terms in Eqs. (4)– (5). The governing equations reduce in this case to

$$\mathrm{i}\omega\tilde{\rho} + \nabla \cdot \left(\tilde{\rho}\,\mathbf{U} + \rho_0\,\tilde{\mathbf{u}}\right) = 0, \tag{D.1}$$

$$\rho_0[\mathrm{D}\tilde{\mathbf{u}} + (\tilde{\mathbf{u}} \cdot \nabla)\mathbf{U}] + \tilde{\rho}\,(\mathbf{U} \cdot \nabla)\mathbf{U} = -\nabla\tilde{p}, \tag{D.2}$$

supplemented by the isentropic relation between pressure and density perturbations. All other conditions are identical to case II: the liner is represented by the impedance boundary condition of Eq. (16), with the frequency-dependent impedance educed from the explicit liner configuration (Section 5), the same computational domain, SPL (145 dB), and bulk Mach number ($M_b = 0.296$).

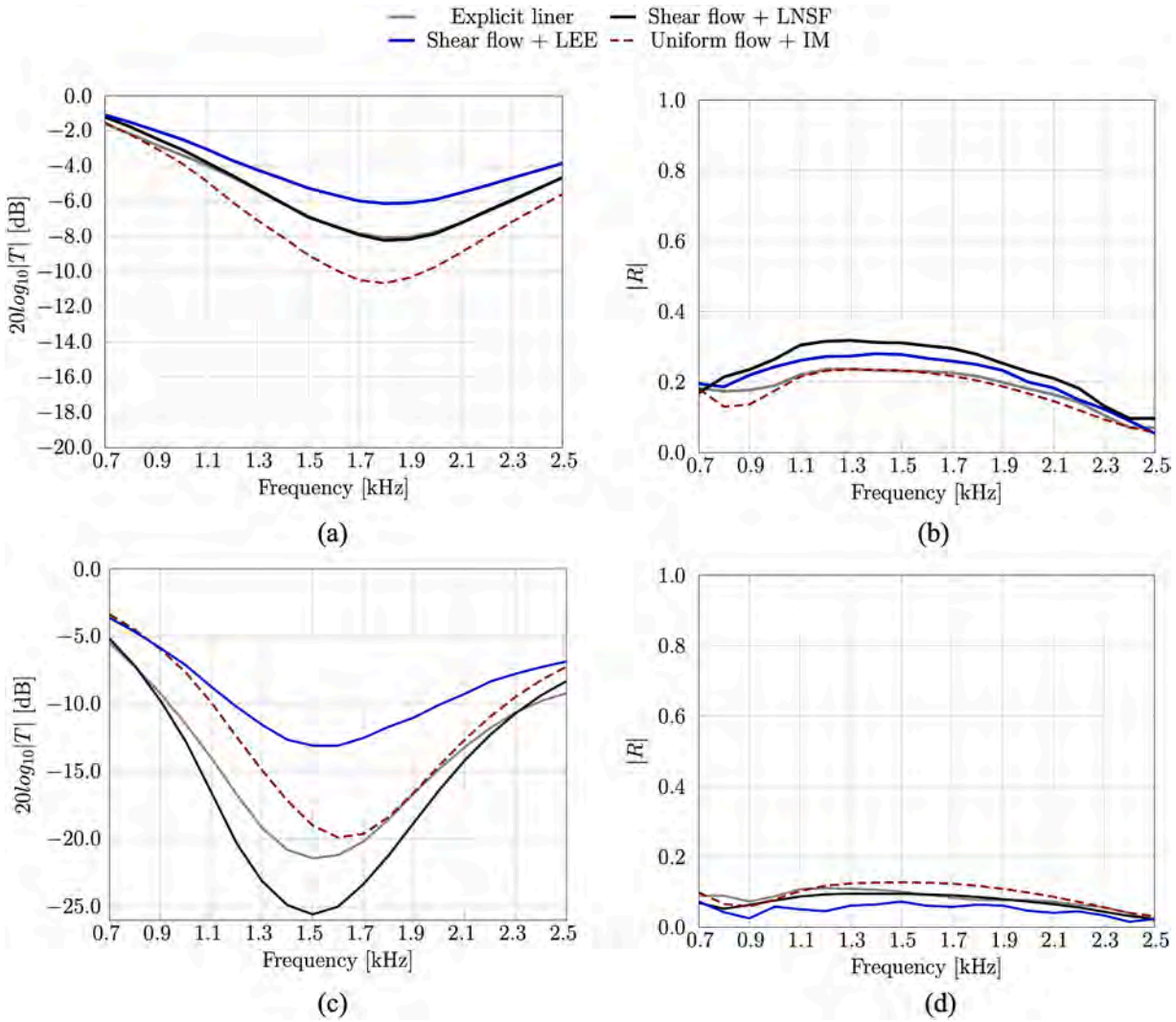


Fig. D.21. Transmission (a, c) and reflection (b, d) coefficients for the impedance-boundary simulations with an upstream acoustic source (a, b) and a downstream acoustic source (c, d).

Fig. D.21 compares the transmission and reflection coefficients of the three impedance-boundary models against the explicit liner simulation, for both upstream and downstream acoustic source locations. The sheared-flow inviscid case exhibits the lowest attenuation of the transmitted wave (the highest $|T|$) among all configurations, while its reflection coefficient remains comparable to the other cases. This behaviour is consistent with the underlying physics: in the LEE formulation, the viscous dissipation associated with the acoustic boundary layer (Section 2.2) is absent, so this contribution to the acoustic attenuation is not included. In the LNSF case, the same dissipation is accounted for by the viscous terms in the governing equations. In the Uniform flow + IM case, the lower transmission does not stem from resolved viscous losses but from the uniform-flow Ingard–Myers treatment of the wall, which redistributes the acoustic energy differently in the absence of a resolved shear profile.

The comparison shows that, for a given impedance, removing viscosity while retaining the sheared profile measurably reduces the attenuation of the transmitted field. Together with the results of Section 5, this confirms that the mean-flow shear profile and the near-wall acoustic viscous effects provide separate, non-negligible contributions to the predicted acoustic response at fixed impedance, and that neither can be regarded as implicitly accounting for the other.

It is worth noting that inviscid sheared formulations are known to admit, in addition to the acoustic modes, hydrodynamic solutions associated with convected vorticity, including a continuous spectrum and possible surface modes over impedance walls [53–55]. However, these hydrodynamic solutions fall outside the scope of the present comparison, which is restricted to the transmitted and reflected fields at fixed impedance and fixed base flow; in the LNSF formulation, in any case, the hydrodynamic solutions are damped by the molecular and turbulent viscosity retained in the governing equations [56].

Table F.4
Comparison of computational cost between the high-fidelity LBM–VLES simulations and the present RANS–LNSF approach.

	High-fidelity (LBM–VLES)	Present approach (RANS–LNSF)
Flow solution	1.64×10^5 CPU h	96 CPU h
Acoustic solution	4.13×10^4 CPU h	24 CPU h
Compute resources	10 nodes (48 cores each)	1 node
Grid size	$\sim 1.1 \times 10^9$ voxels	FEM mesh ($\sim 10^6$ elements)
DOF (acoustic solution)	$\approx 19 \times 10^9$	$\approx 8 \times 10^6$

Appendix E. The effect of different impedance values

To provide an additional level of validation of the numerical framework, the transmission and reflection coefficients are recomputed using the impedance values educed in Fig. 5 and compared against the reference solution obtained from the explicit liner simulation. In particular, the impedances educed for both upstream- and downstream-source configurations are imposed as boundary conditions, and the resulting acoustic fields are analysed for a downstream acoustic source.

By construction, the eduction process compresses the complex interaction between the mean flow, viscous effects, and acoustic field into a single frequency-dependent quantity. The educed impedance should therefore be interpreted as an effective parameter that incorporates the combined influence of the flow–acoustic coupling mechanisms occurring within and above the liner.

The results show that the impedance obtained for the downstream-source configuration reproduces the frequency-dependent behaviour of both the transmission and reflection coefficients with good agreement when compared to the explicit liner simulation, as illustrated in Fig. E.22.

Overall, this comparison supports the interpretation of the educed impedance as an effective quantity that captures the integral response of the coupled flow–acoustic system, while demonstrating its ability to reproduce the main scattering characteristics of the liner under consistent propagation conditions.

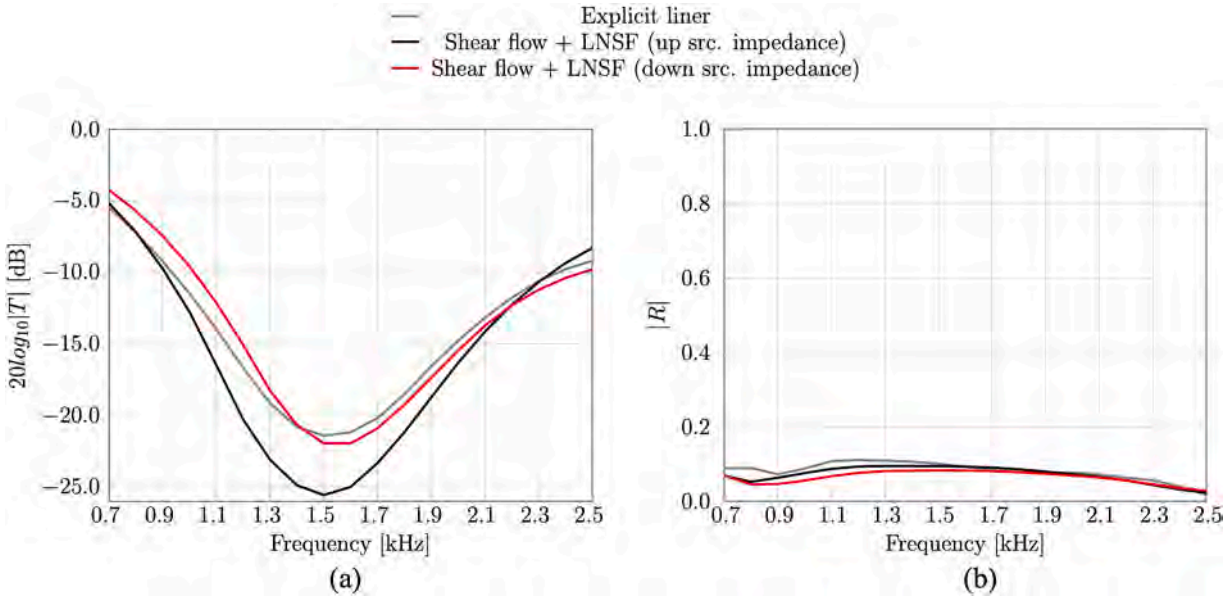


Fig. E.22. Transmission (a) and reflection (b) coefficients obtained from impedance-boundary simulations for different imposed impedance values, compared with the explicit liner simulation for a downstream acoustic source.

Appendix F. Computational resources

To provide a quantitative comparison of the computational effort, Table F.4 summarises the cost of the high-fidelity LBM–VLES simulations and of the present RANS–LNSF framework. Table F.4 reports the CPU-hours for the present setup compared with the high-fidelity data, together with the number of degrees of freedom (DOF) of both simulations. It is important to note that the comparison is carried out for the case where the liner is explicitly resolved.

The high-fidelity simulation grid is the one presented in Paduano et al. [5]. The acoustic cost of 24 CPU h reported in the table corresponds to a single forward LNSF solve for the explicit liner simulation. The complete eduction, in which the liner is modelled

through an impedance boundary condition, requires on average 159 forward solves per frequency; each solve takes about 30 s on 48 cores, resulting in a total cost of approximately 1200 CPU h for the 19 frequencies considered. The simulation required a peak of approximately 80 GB of RAM. Most of this was used by the matrix factorisation in the direct solver, while matrix assembly needed only about 5 GB.

Appendix G. Eduction method

To assess whether the educed impedance is sensitive to the chosen search domain, we performed two checks. First, we repeated the eduction at representative frequencies using a substantially enlarged initial domain ($\theta \in [0.01, 6]$, $\chi \in [-8, 8]$). The educed values agree closely with those obtained using the standard bounds, with a maximum difference of 0.09 in resistance at $f = 1600$ Hz and negligible differences elsewhere, indicating that the results are largely insensitive to the initial search domain. Second, Fig. G.23 shows the residual landscape $\mathrm{Res}(\theta, \chi)$ at a representative frequency. Within the search domain it exhibits a single, well-defined minimum, which suggests that the inverse problem is well-conditioned in this region and that the educed solution is not an artefact of local minima.

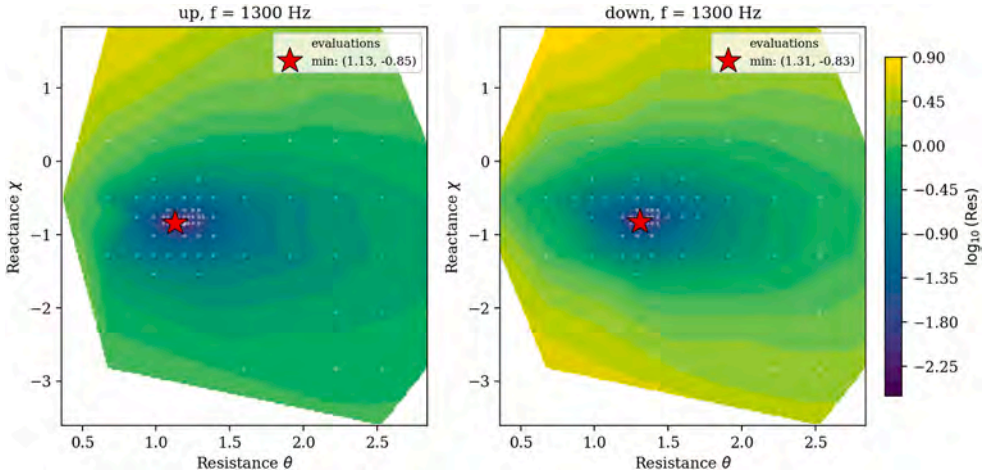


Fig. G.23. Residual landscape $\mathrm{Res}(\theta, \chi)$ of the eduction objective (Eq. (22)) at $f = 1300$ Hz, for two different acoustic source location. The red star marker indicates the educed impedance. (For interpretation of the references to colour in this figure legend, the reader is referred to the web version of this article.)

References

[1] T. Zandbergen, Do locally reacting acoustic liners always behave as they should?, AIAA J. 18 (4) (1980) 396–397. https://doi.org/10.2514/3.50771
[2] O. Léon, F. Méry, E. Piot, C. Conte, Near-wall aerodynamic response of an acoustic liner to harmonic excitation with grazing flow, Exp. Fluids 60 (9) (2019). https://doi.org/10.1007/s00348-019-2791-5
[3] P.D. Dean, An in Situ Method of Wall Acoustic Impedance Measurement in Flow Ducts, Technical Report 1, 1974.
[4] L.A. Bonomo, N.T. Quintino, A.M.N. Spillere, J.A. Cordioli, P.B. Murray, A comparison of in-situ and impedance eduction experimental techniques for acoustic liners with grazing flow and high SPL, in: 28th AIAA/CEAS Aeroacoustics Conference, 2022, 2022. https://doi.org/10.2514/6.2022-2998
[5] A. Paduano, F. Scarano, J. Cordioli, D. Casalino, F. Avallone, On the impact of the turbulent grazing flow development on the acoustic response of an acoustic liner, J. Fluid Mech. 1035 (2026) A11, https://doi.org/10.1017/jfm.2026.11544
[6] U. Ingard, Influence of fluid motion past a plane boundary on sound reflection, absorption, and transmission, J. Acoust. Soc. Am. 31 (7) (1959) 1035–1036. https://doi.org/10.1121/1.1907805
[7] M.K. Myers, On the acoustic boundary condition in the presence of flow, J. Sound Vib. 71 (3) (1980). https://doi.org/10.1016/0022-460X(80)90424-1
[8] W. Eversman, R.J. Beckemeyer, Transmission of sound in ducts with thin shear layers—convergence to the uniform flow case, J. Acoust. Soc. Am. 52 (1B) (1972) 216–220. https://doi.org/10.1121/1.1913082
[9] N.T. Quintino, L.A. Bonomo, J.A. Cordioli, M.G. Jones, B.M. Howerton, D.M. Nark, F. Avallone, Comparison of impedance eduction test rigs with different boundary-layer profiles, AIAA J. 63 (11) (2025) 4872–4883.
[10] A.H. Nayfeh, J.E. Kaiser, B.S. Shaker, Effect of mean-velocity profile shapes on sound transmission through two-dimensional ducts, J. Sound Vib. 34 (3) (1974) 413–423. https://doi.org/10.1016/S0022-460X(74)80320-2
[11] G. Gabard, Boundary layer effects on liners for aircraft engines, J. Sound Vib. 381 (2016) 30–47. https://doi.org/10.1016/j.jsv.2016.06.032
[12] G. Gabard, A comparison of impedance boundary conditions for flow acoustics, J. Sound Vib. 332 (4) (2013) 714–724. https://doi.org/10.1016/j.jsv.2012.10.014
[13] E.J. Brambley, Well-Posed boundary condition for acoustic liners in straight ducts with flow, AIAA J. 49 (6) (2011) 1272–1282. https://doi.org/10.2514/1.J050723
[14] A.M.N. Spillere, L.A. Bonomo, J.A. Cordioli, E.J. Brambley, Experimentally testing impedance boundary conditions for acoustic liners with flow: beyond upstream and downstream, J. Sound Vib. 489 (2020). https://doi.org/10.1016/j.jsv.2020.115676
[15] Y. Renou, Y. Aurégan, et al., Failure of the Ingard–Myers boundary condition for a lined duct: an experimental investigation, J. Acoust. Soc. Am. 130 (1) (2011) 52–60. https://doi.org/10.1121/1.3586789
[16] Y. Aurégan, R. Starobinski, V. Pagneux, Influence of grazing flow and dissipation effects on the acoustic boundary conditions at a lined wall, Acoust. Soc. Am. J. 109 (2001) 59–64. https://doi.org/10.1121/1.1331678
[17] H. Shahzad, S. Hickel, D. Modesti, Direct numerical simulation of a turbulent boundary layer over acoustic liners, American Institute of Aeronautics and Astronautics (AIAA), 2023. https://doi.org/10.2514/6.2023-3887
[18] D. Khamis, E.J. Brambley, The effective impedance of a finite-thickness viscothermal boundary layer over an acoustic lining, https://doi.org/10.2514/6.2015-2229
[19] D. Khamis, E.J. Brambley, Acoustic boundary conditions at an impedance lining in inviscid shear flow, J. Fluid Mech. 796 (2016) 386–416. https://doi.org/10.1017/jfm.2016.273
[20] Q. Zhang, D.J. Bodony, Numerical investigation of a honeycomb liner grazed by laminar and turbulent boundary layers, J. Fluid Mech. 792 (2016) 936–980. https://doi.org/10.1017/jfm.2016.79

[21] R. Roncen, F. Méry, E. Piot, P. Klotz, Spatially-varying impedance model for locally reacting acoustic liners at a high sound intensity, J. Sound Vib. 524 (2022) 116741. https://doi.org/10.1016/j.jsv.2021.116741
[22] C. Weng, A. Schulz, D. Ronneberger, L. Enghardt, F. Bake, Flow and viscous effects on impedance eduction, AIAA J. 56 (3) (2018) 1118–1132. https://doi.org/10.2514/1.J055838
[23] C.K.W. Tam, K.A. Kurbatskii, Microfluid dynamics and acoustics of resonant liners, AIAA J. 38 (8) (2000) 1331–1339. https://doi.org/10.2514/2.1132
[24] F. Menter, M. Kuntz, R.B. Langtry, Ten year of industrial experience with the SST turbulence model, in: Proceedings of the 4th International Symposium on Turbulence, Heat and Mass Transfer, Begell House, Inc., Redding, (2003) 625–632.
[25] W.C. Reynolds, A.K.M.F. Hussain, The mechanics of an organized wave in turbulent shear flow. Part 3. Theoretical models and comparisons with experiments, J. Fluid Mech. 54 (2) (1972) 263–288. https://doi.org/10.1017/S0022112072000679
[26] A. Holmberg, A. Kierkegaard, C. Weng, A frequency domain linearized Navier–Stokes method including acoustic damping by eddy viscosity using RANS, J. Sound Vib. 346 (2015) 229–247. https://doi.org/10.1016/j.jsv.2015.02.030
[27] F. Scarano, A. Paduano, F. Avallone, Noise dissipation mechanisms of an acoustic liner under grazing flow, J. Fluid Mech. 1038 (2026) A21. https://doi.org/10.1017/jfm.2026.11759
[28] C.K.W. Tam, N.N. Pastouchenko, M.G. Jones, W.R. Watson, Experimental validation of numerical simulations for an acoustic liner in grazing flow: self-noise and added drag, J. Sound Vib. 333 (2014). https://doi.org/10.1016/j.jsv.2014.02.019
[29] M. Berggren, A. Bernland, D. Noreland, Acoustic boundary layers as boundary conditions, J. Comput. Phys. 371 (2018) 633–650. https://doi.org/10.1016/j.jcp.2018.06.005
[30] F.Q. Hu, A stable, perfectly matched layer for linearized Euler equations in unsplit physical variables, J. Comput. Phys. 173 (2) (2001) 455–480. https://doi.org/10.1006/jcph.2001.6887
[31] A. Kierkegaard, S. Boij, G. Efraimsson, A frequency domain linearized Navier–Stokes equations approach to acoustic propagation in flow ducts with sharp edges, J. Acoust. Soc. Am. 127 (2) (2010) 710–719. https://doi.org/10.1121/1.3273899
[32] V.T. H. V.T. Hoang, A. Jafari, B. Cazzolato, M. Arjomandi, Impacts of acoustic impedance of a perforated plate on near-wall turbulence, Phys. Fluids 37 (2) (2025) 025102. https://doi.org/10.1063/5.0249382
[33] T. Elnady, H. Bodén, An inverse analytical method for extracting liner impedance from pressure measurements, in: Collection of Technical Papers - 10th AIAA/CEAS Aeroacoustics Conference, 1, 2004. https://doi.org/10.2514/6.2004-2836
[34] J. Yu, M. Ruiz, H.W. Kwan, Validation of Goodrich perforate liner impedance model using NASA langley test data, in: 14th AIAA/CEAS Aeroacoustics Conference (29th AIAA Aeroacoustics Conference), 2008. https://doi.org/10.2514/6.2008-2930
[35] T.H. Melling, The Acoustic Impedance of Perforates at Medium and High Sound Pressure Levels, Technical Report 1, 1973.
[36] F. Avallone, A. Paduano, L.M. Pereira, L.A. Bonomo, J.A. Cordioli, D. Casalino, D. Cerizza, On the comparison of different methods for impedance eduction applied to a numerical database, Torino, 2024.
[37] R.L. Panton, J.M. Miller, Resonant frequencies of cylindrical Helmholtz resonators, J. Acoust. Soc. Am. 57 (6) (1975) 1533–1535. https://doi.org/10.1121/1.380596
[38] M.G. Jones, M.B. Tracy, W.R. Watson, T.L. Parrott, Effects of liner geometry on acoustic impedance, in: 8th AIAA/CEAS Aeroacoustics Conference and Exhibit, American Institute of Aeronautics and Astronautics Inc., 2002. https://doi.org/10.2514/6.2002-2446
[39] J. Jiménez, Turbulent flows over rough wall, Annu. Rev. Fluid Mech 36 (2004) 173–96. https://doi.org/10.1146/annurev.fluid.36.050802.122103
[40] C. Saverna, Y. Aurégan, V. Pagneux, Non-reciprocal scattering in shear flow, J. Acoust. Soc. Am. 146 (2) (2019) 1051–1060. https://doi.org/10.1121/1.5120523
[41] L.A. Bonomo, A.M.N. Spillere, J.A. Cordioli, E.J. Brambley, Optimal impedance of a lined plane surface with inviscid sheared grazing flow, J. Sound Vib. 595 (2025) 118659. https://doi.org/10.1016/j.jsv.2024.118659
[42] J.M. Gablonsky, C.T. Kelley, A locally-biased form of the DIRECT algorithm, J. Glob. Optim. 21 (2001) 27–37. https://doi.org/10.1023/a:1017930332101
[43] D. Cerizza, D. Casalino, An indirect impedance eduction process for liners with arbitrarily complex geometry, 2023. https://doi.org/10.2514/6.2023-4186
[44] T.H. Rowan, Functional Stability Analysis of Numerical Algorithms, Ph.D. thesis, Department of Computer Science, University of Texas at Austin, Austin, TX, 1990.
[45] C. Weng, A. Schulz, D. Ronneberger, L. Enghardt, F. Bake, Impedance eduction in the presence of turbulent shear flow using the linearized Navier-Stokes equations, https://doi.org/10.2514/6.2017-3182
[46] L.A. Bonomo, A.M.N. Spillere, J.A. Cordioli, Parametric uncertainty analysis for impedance eduction based on Prony's method, AIAA J. 58 (8) (2020). https://doi.org/10.2514/1.J059071
[47] H. Rashidi, J. Golliard, T. Humbert, 3D multimodal inverse method for liner impedance eduction, J. Sound Vib. 605 (2025) 118954. https://doi.org/10.1016/j.jsv.2025.118954
[48] S.W. Rienstra, A. Hirschberg, An Introduction to Acoustics, Eindhoven University of Technology, 2004.
[49] M.L. Munjal, Acoustics of Ducts and Mufflers, John Wiley & Sons, Chichester, 2nd ed., 2014.
[50] G.H. Golub, C.F. Van Loan, Matrix Computations, Johns Hopkins University Press, Baltimore, 4th ed., 2013.
[51] H. Bodén, M. Åbom, Influence of errors on the two-microphone method for measuring acoustic properties in ducts, J. Acoust. Soc. Am. 79 (2) (1986) 541–549. https://doi.org/10.1121/1.393542
[52] M. Åbom, H. Bodén, Error analysis of two-microphone measurements in ducts with flow, J. Acoust. Soc. Am. 83 (6) (1988) 2429–2438. https://doi.org/10.1121/1.396322
[53] E.J. Brambley, Fundamental problems with the model of uniform flow over acoustic linings, J. Sound Vib. 322 (4) (2009) 1026–1037. https://www.sciencedirect.com/science/article/pii/S0022460X08009309. https://doi.org/10.1016/j.jsv.2008.11.021
[54] S.W. Rienstra, M. Darau, Boundary-layer thickness effects of the hydrodynamic instability along an impedance wall, J. Fluid Mech. 671 (2011) 559–573. https://doi.org/10.1017/S0022112010006051
[55] L.A. Bonomo, J.A. Cordioli, E.J. Brambley, A. Paduano, F. Avallone, Realistic sheared flow profile effects on acoustic impedance eduction in small three-dimensional ducts, AIAA J. 0 (0) (0) 1–10. 10.2514/1.J066637. https://doi.org/10.2514/1.J066637
[56] D. Marx, Y. Aurégan, Effect of turbulent eddy viscosity on the unstable surface mode above an acoustic liner, J. Sound Vib. 332 (15) (2013) 3803–3820. https://doi.org/10.1016/j.jsv.2013.02.005